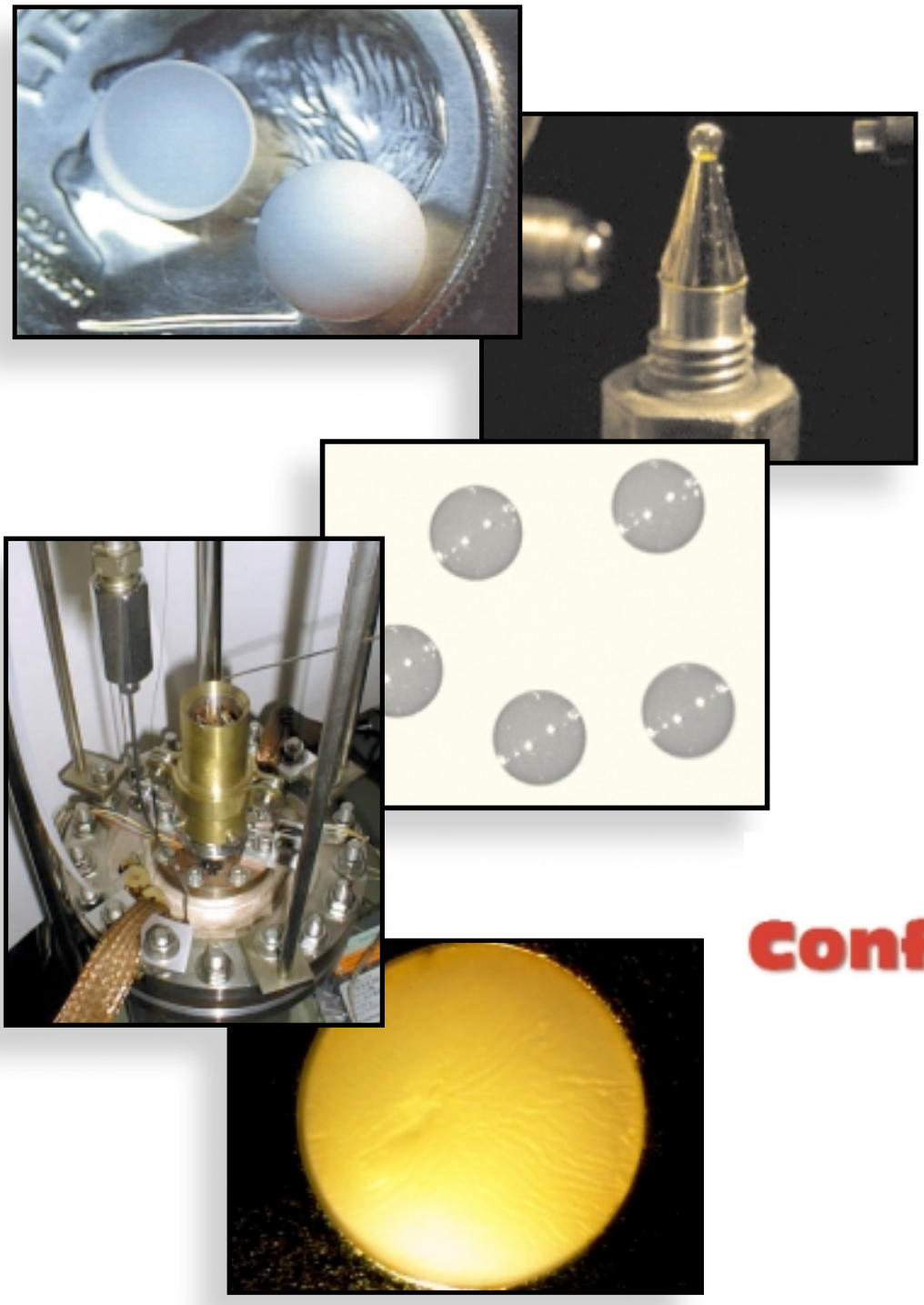

Inertial Confinement Fusion

ANNUAL REPORT

OCTOBER 1, 1999
THROUGH
SEPTEMBER 30, 2000

Schafer

GENERAL ATOMICS

DISCLAIMER

GA–A23537

INERTIAL CONFINEMENT FUSION TARGET COMPONENT FABRICATION AND TECHNOLOGY DEVELOPMENT SUPPORT

ANNUAL REPORT TO THE U.S. DEPARTMENT OF ENERGY

OCTOBER 1, 1999 THROUGH SEPTEMBER 30, 2000

by
PROJECT STAFF

Work prepared under
Department of Energy
Contract No. DE-AC03-95SF20732

GENERAL ATOMICS PROJECT 03748
DATE PUBLISHED: JANUARY 2001

THE FY00 TARGET FABRICATION AND TARGET TECHNOLOGY DEVELOPMENT TEAM

Dr. Kenneth Schultz
Program Manager

General Atomics
San Diego, California

Neil Alexander, Wes Baugh, Chandu Baxi, Chuck Beal, Gottfried Besenbruch, Karl Boline, Lloyd Brown, Erwin Castillo, Chuck Charman, Sharon Considine, Don Czechowicz, Vic Delbene, Fred Elsner, Dana Forster, Chuck Gibson, Jane Gibson, Kett Gifford, Dan Goodin, Steve Grant, Annette Greenwood, Martin Hoppe, Dave Husband, Jim Kaae, Buelah Koz, Jim Kulchar, Barry McQuillan, Wayne Miller, Abbas Nikroo, Sally Paguio, Joe Pontelandolfo, Elmer Reis, John Ruppe, Chuck Schneidmuller, Clyde Shearer, John Sheliak, Joe Smith, Dave Steinman, Bob Stemke, Rich Stephens, John Vanderzanden, Don Wall, Jason Wall, David Woodhouse

Schafer Corporation
Livermore, California

Thom Bahrs, Allen Bohart, Don Bittner, John Burmann, Sue Carter, Pat Collins, Steve Dropinski, Illges Faron, Scott Faulk, Kett Gifford, Craig Halvorson, Ed Hsieh, Lisa MacGregor, Derrick Mathews, Michael Monsler, Brian Motta, Ron Perea, Craig Rivers, Jim Sater, Diana Schroen-Carey, Keith Shillito, Cheryl Spencer, Katie Strube, Alicia Thomas, Tom Walsh, Kelly Youngblood

ABSTRACT

General Atomics (GA) has served as the Inertial Confinement Fusion (ICF) Target Component Fabrication and Technology Development Support contractor for the U.S. Department of Energy since December 30, 1990. This report documents the technical activities of the period October 1, 1999 through September 30, 2000.

During this period, GA and our partner Schafer Corporation were assigned 16 formal tasks in support of the ICF program and its five laboratories. A portion of the effort on these tasks included providing direct "Onsite Support" at Lawrence Livermore National Laboratory (LLNL), Los Alamos National Laboratory (LANL), and Sandia National Laboratory (SNL). We fabricated and delivered over 1250 hohlraum mandrels and numerous other micromachined components to LLNL, LANL, and SNL. We produced more than 1250 glass and plastic target capsules over a wide range of sizes and designs (plus over 750 near target-quality capsules and over 1500 sample shells) for LLNL, LANL, SNL, and University of Rochester/Laboratory for Laser Energetics (UR/LLE). We also delivered various target foils and films for Naval Research Lab (NRL) and UR/LLE in FY00. We fabricated a device to polish NIF-sized beryllium shells and prepared a laboratory for the safe operation of beryllium polishing activities. This report describes these target fabrication activities and the target fabrication and characterization development activities that made the deliveries possible.

The ICF program is anticipating experiments at the OMEGA laser and the National Ignition Facility (NIF) which will require targets containing cryogenic layered D_2 or deuterium-tritium (D-T) fuel. We are part of the National Cryogenic Target Program and support experiments at LLNL and LANL to generate and characterize cryogenic layers for these targets. We also contributed cryogenic engineering support and developed concepts for NIF cryogenic targets. This report summarizes and documents the technical progress made on these tasks.

ACRONYMS

AFM	atomic force microscope
CPL	cryogenic pressure loader
CTM	cryogenic target mount
CTS	cryogenic target system
D_2TS	deuterium test system
D-T	deuterium-tritium
DVB	divinyl benzine
E-CTFE	ethylene-chlorotrifluoroethylene
EOS	equation of state
FO	facility operator
FP	field point
GDP	glow discharge polymer
GA	General Atomics
H-D	hydrogen-deuterium
ICF	Inertial Confinement Fusion
ICS	instrumentation and control system
IPE	di-isopropylether
IR	infrared
ISO	inside-out
LANL	Los Alamos National Laboratory
LCS	local control system
LCTS	LMJ Cryogenic Target System
LEH	laser entrance hole
LLNL	Lawrence Livermore National Laboratory
LMJ	Laser Megajoules
NCTS	NIF Cryogenic Target System
NIF	National Ignition Facility

NRL	Naval Research Laboratory
OOR	out-of-round (difference in major and minor radius of a best fit ellipse)
OCTS	OMEGA Cryogenic Target System
PAA	polyacrylic acid
PAMS	poly(α-methylstyrene)
PCHMS	permeation cell housing and motion system
PCPR	permeation cell plug remover
PCSCS	permeation cell support and cooling system
PLL	phase locked loop
PS	polystyrene
PVA	poly(vinylalcohol)
REH	radiation entry hole
rf	radio frequency
RF	resorcinol-formaldehyde
RSO	right-side-out
SEM	scanning electron microscope
Si-PS	silicon-doped polystyrene
SiGDP	silicon-doped glow discharge polymer
SNL	Sandia National Laboratory
T2B	trans-2-butene
TIC	target insertion cryostats
TPX	commercial designation of the polymer produced by the polymerization of 1-methyl-4-pentene
TWTS	tritium waste treatment system
UR/LLE	University of Rochester/Laboratory for Laser Energetics
W2	outer water solution
XRF	x-ray fluorescence

TABLE OF CONTENTS

LIST OF FIGURES

LIST OF TABLES

1. TARGET FABRICATION PROGRAM OVERVIEW

General Atomics (GA) has served as the Inertial Confinement Fusion (ICF) Target Component Fabrication and Technology Development Support contractor for the U.S. Department of Energy since December 30, 1990. This report documents the technical activities of the period October 1, 1999 through September 30, 2000. GA was assisted by Schafer Corporation and we have carried out the ICF Target Fabrication tasks as a fully integrated team effort.

During FY00, the GA/Schafer team was assigned 16 formal tasks as shown in Table 1–1. These tasks are described briefly here (Section 1). Additional technical detail on selected topics is given in Sections 2 through 7 of this report.

TABLE 1–1
FY00 TARGET FABRICATION TASKS

Task No.	Task Title Description	Total $K	Task Leader
LL01	Onsite Support for LLNL	500	Miller
LL02	Micromachined Target Components	925	Kaae
LL03	Composite Polymer Capsules for LLNL	780	Miller
LA01	Onsite Support for LANL	181	Shillito
LA02	Composite Polymer Capsules for LANL	445	Miller
LA03	Beryllium Shell Support for LANL	71	Brown
NR01	NRL Target Deliveries	1165	Walsh
SL01	Target Components and Capsules for SNL	586	Kaae
SL02	Target Fabrication for SNL	685	Schroen-Carey
UR01	Target Production and Delivery for LLE	1600	Miller
UR02	Cryogenic Capsule Development	200	Nikroo
UR03	Flat Foils	145	Walsh
CR/LL1	Enhanced Cryo. Target Fielding Development	635	Sater
CR/LL2	NIF Cryogenic Target System Development	1090	Alexander
CR/LA1	Beta Layering Support at LANL	221	Sheliak
CR/UR1	OMEGA Cryo. Target System Engineering	85	Besenbruch
	Total	$9,314	

1.1. LL01 ONSITE SUPPORT FOR LLNL

Our onsite team at Lawrence Livermore National Laboratory (LLNL) was composed of Kett Gifford (May through September), Derrick Mathews (October through May), Craig Rivers, and John Ruppe. They provided support in micromachining of target components, assembling target components into complete targets, and characterizing target components and capsules for use in NOVA and OMEGA ICF experiments. With the shutdown of NOVA, support was required at OMEGA during some of the LLNL experimental series. Both Gifford and Ruppe spent time at OMEGA providing that support.

1.2. LL02 MICROMACHINED TARGET COMPONENTS

This year we fabricated 1170 micromachined target components in this task for both LLNL and Los Alamos National Laboratory (LANL), the majority of which went to LLNL. Two hundred and forty (240) of these components were conventional copper hohlraum mandrels of different sizes coated with a single layer of gold, 310 were conventional copper hohlraum mandrels of various sizes coated with a thin layer of gold and a thicker layer of epoxy, 12 were gold double-walled hohlraums on copper mandrels, 210 were aluminum witness plates with various profiles, 100 were copper witness plates with various profiles, and the remainder were various other components. Among the latter were copper hohlraum mandrels with roughened surfaces plated with gold, flat copper disks, gold tubes, top-hat shaped plates, sine wave profiles in polyimide, epoxy tubes, hollow gold spindles, sine wave profiles in gold plated on polystyrene (PS), spherically shaped copper hohlraum mandrels plated with gold, square shaped copper mandrels plated with gold, gold trapezoidally shaped shields, gold disks with a controlled roughness on one-half of one of the faces, sine wave profiles in copper, and triangular and flat profiles in gold.

1.3. LL03/LA02/UR01 COMPOSITE POLYMER CAPSULES

The chief purpose of the capsule tasks is to supply target-quality capsules for current experiments. This past year, the experimental needs required considerable flexibility in diameters, materials, and layer thickness. As can be seen in Fig. 1.3–1, we delivered capsules with diameters ranging between 200 and 5000 μm and total wall thicknesses ranging between 2 and 150 μm. The capsules consisted of glass shells, polymer capsules of up to four layers, glow discharge polymer (GDP)-coated glass shells, and polymer hemispheres. At least one of the layers in a multilayer capsule was doped with deuterium, chlorine, silicon, titanium, or germanium. Some of the capsules were filled with fuel or diagnostic gas.

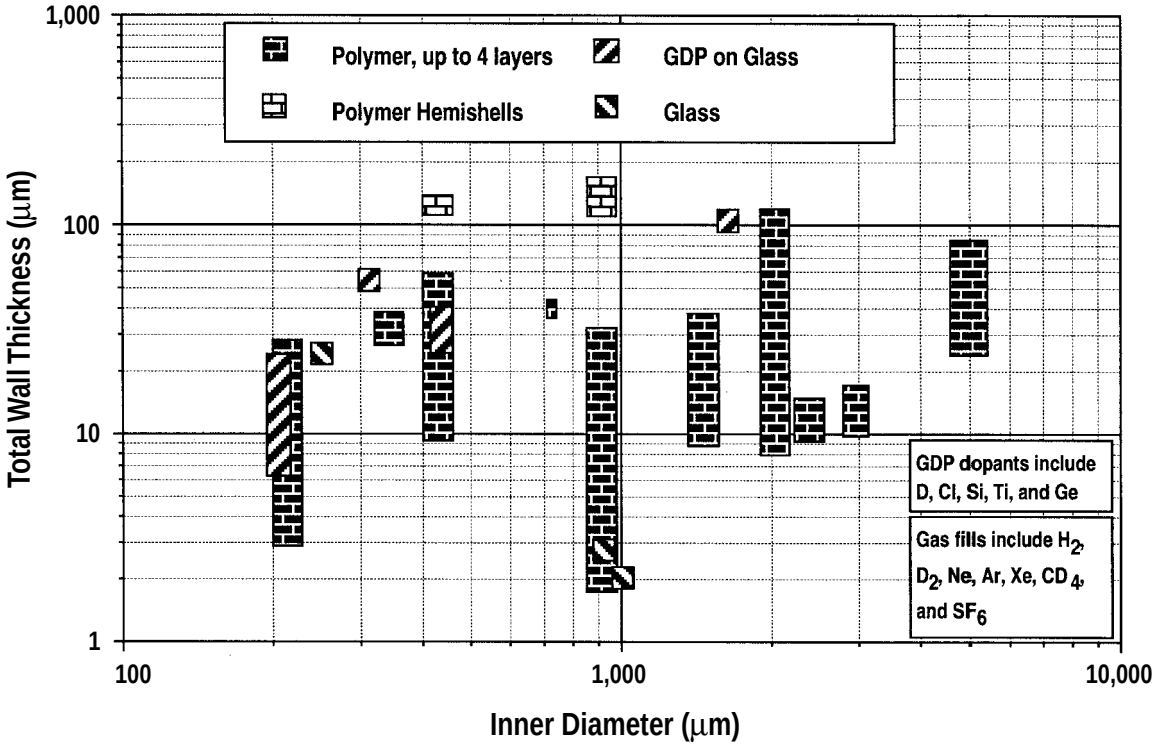

Fig. 1.3–1. GA delivered a wide range of capsule sizes and capsule types to support current experiments in the national ICF program.

Overall, we shipped 84 orders, for a total of over 1250 target-quality, thoroughly characterized capsules. In addition, we shipped over 730 less thoroughly characterized capsules and over 1500 samples of a variety of types.

The second goal of the capsule tasks is to make improvement in techniques that increase the quality, size ranges, material properties, and characterization of the capsules or decrease the cost of fabrication. We improved our capabilities in several respects:

- *Poly(α-methylstyrene) (PAMS) shell mandrels for National Ignition Facility (NIF) targets (~2 mm diameter) approach NIF quality*. The mandrels now meet the NIF standard for the power modes, but when coated produce a GDP surface finish that has unacceptable power at the higher modes. The GDP deposition process tends to accentuate tiny surface imperfections. The power of the high modes for a PAMS mandrel must be far enough below the NIF standard to allow GDP deposited on the mandrel to have NIF-quality power modes. We are working on further improving the high mode surface finish of the PAMS mandrels. GA supported LLNL employee Masaru Takagi in the development of the PAMS mandrels for NIF.
- *PAMS mandrels below 1 mm diameter used for current experiments now have much lower "mode 10" surface finish power*. By controlling what we believe are

Marangoni flow cells during shell formation, we dramatically reduced the large values around mode 10 so that the mandrels routinely meet or beat the NIF power curve standard.

- *We found conditions to make much stronger and more permeable polymer capsules for cryogenic experiments on OMEGA by changing the GDP deposition conditions*. This polymer has a much higher density (we measured up to 1.4 g/cm^3). The higher density may make the polymer suitable for use in NIF capsules.
- *We improved the yield of shells coated with poly(vinylalcohol) (PVA)*. Previously, only 2% of the shells ended up as target quality PVA-coated shells. We made changes to the deposition process that have provided as much as 17% yield.
- *We improved our characterization techniques*. We now provide better measurements of permeability, density, surface finish (spheremapper), and wall thickness variations (wallmapper). We also found that polarized light can be used to examine rapidly the entire capsule for surface anomalies.

The improvements are discussed in detail in Section 2.

1.4. LA01 ONSITE SUPPORT FOR LANL

We provided one technician to give onsite support for LANL under this task. There was no support provided at LLNL as in previous years. At LANL, Ron Perea provided onsite support for target machining, assembly, and characterization of targets that were shot at Trident, Z, and OMEGA. He has worked independently with the Trident experimenters, iterating designs (preparing CAD target drawings), fabricating and assembling parts, and characterizing completed targets. Ron provided assistance during LANL target campaigns at the University of Rochester/Laboratory for Laser Energetics (UR/LLE) on two separate occasions during the year. More than 900 targets were delivered during the year comprised of many design variations and materials combinations.

1.5. LA03 BERYLLIUM SHELL SUPPORT FOR LANL

This work in this task is divided into two subtasks: (1) characterization of specimens provided by LANL, and (2) development of polishing techniques applicable to beryllium targets.

Two types of characterization were carried out: spheremapping of commercial ball bearings and radiographic analysis of beryllium braze samples. We spheremapped

Grade 3 ball bearings, obtained by LANL through commercial sources, to determine the quality of readily available metallic spheres. The Grade 3 bearings were shown to meet the NIF standards for sphericity and smoothness (Fig. 1.5–1).

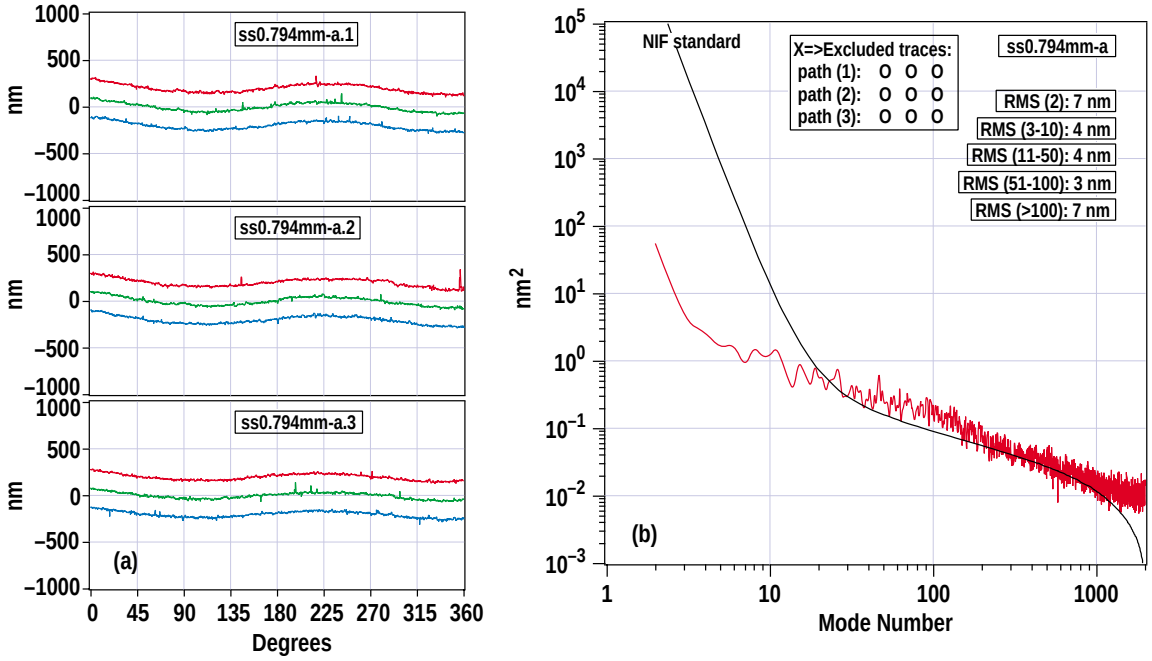

Fig. 1.5–1. Atomic force microscope (AFM) spheremap traces and mode map of Grade 3 ball bearing.

Sixteen braze samples were investigated via radiography. From 1 to 3 radiographs were taken of each sample for a total of 31 radiographs. Overall analysis and correlation of the results is being carried out by LANL but, generally, samples either showed a significant amount of braze material left in the joint or had gaps in the joint. No sample showed complete Be-Be bonding with the braze material fully diffused into the bulk.

The polishing effort was to investigate polishing of NIF sized spheres, first using surrogate spheres and then using beryllium spheres supplied by LANL. In consultation with both LANL and LLNL, titanium was selected as the surrogate material of choice for simulation of beryllium polishing. We located a supplier, New England Miniature Ball, who was willing to make on a lot of 2-mm titanium spheres suitable for testing the polishing apparatus. The spheres were made to the Class 100 specification (130 nm surface roughness, etc.) with the additional constraint that the sphericity be that of Class 48 (1.2 μm). About this time, the results of spheremapping commercial Grade 3 ball bearings became available and LANL directed that the laboratory effort on polishing be deferred until commercial polishing techniques could be reevaluated.

1.6. NR01/UR03 NIKE TARGET DEVELOPMENT AND DELIVERIES

The NR01 task target requirements are similar to those of past years. We have provided flat film PS targets that are flat and either smooth or rippled with a specified pattern. We have also provided cryogenic targets in a variety of configurations. Many cryogenic targets are merely a cryogenic target mount (CTM) with 1.5 μm polyimide stretched across the top to act as a cryopressure seal. Others are CTMs with polyimide and foam. The foam may be resorcinol-formaldehyde, PS, or other low-density CH material. Foams have been smooth or patterned and have been mounted on smooth or patterned polyimide. Finally, we have developed and delivered cryogenic equation-of-state targets that are composed of layers of aluminum, plastic, and foam in various configurations.

We have improved our characterization capability this past year by adding a scanning white light profilometer to our characterization suite. We have also improved the cleanliness of the targets we make by adding more modular clean room space and filtering the air that comes into our labs.

1.7. SL01 COMPONENTS AND CAPSULES FOR SNL

We fabricated 85 micromachined components of 11 different kinds this year on this task. Of these, four were aluminum plates of various designs, two were thin-walled copper cylinders, four were PS foam spheres (foam sphere production is described in Section 4), and one was a GDP-coated copper hemispherical mandrel.

We also developed micromachining techniques for fabricating PS foam shells, the details of which are described in Section 3.1.

We delivered a total of six 2-mm target-quality capsules to Sandia National Laboratory (SNL) for experiments on the Z-pinch machine. These capsules had nominal 60-μm thick walls of dopant-free GDP coated with about 4 μm of PVA. In addition, we delivered several samples: three 5 mm PAMS shells, 6 GDP-coated PAMS shells, and eight 2 mm × 13 μm GDP shells. We are continuing to develop the dip-coating technique for depositing PVA (see Section 2 for details).

1.8. SL02 FOAM TARGETS FOR SNL

This task is composed of two subtasks: (1) onsite support of one full-time technician, and (2) low-density foams and machining. The onsite support position was very capably handled by Steve Dropinski. Mr. Dropinski was instrumental in working with the experimenters to get new target designs fielded to very demanding tolerances. Often this

required the development of new techniques and the designing of fixtures and precision presses.

The low-density foams were produced at two facilities: (1) Schafer Livermore cleanroom foam laboratory, and (2) an onsite laboratory at SNL. At the Schafer facility, with the support of the adjoining machine shop and coating laboratory, we did mold development for the foam components, produced standard runs of foam components, and produced gold coated. At the SNL laboratory, we developed new foam processes and produced foam components too fragile to ship.

1.9. UR02 CRYOGENIC CAPSULE DEVELOPMENT

Under this task, we continued our investigation of making thin walled (≈1 μm thick, 900 μm diameter) GDP capsules using the GDP/PAMS process for LLE cryogenic experiments. We explored many different parameters involved in making such shells. In particular, we varied many of the GDP deposition parameters to determine the ideal conditions for making the strongest shells. 1.5 μm thick GDP shells with Young's moduli of over 2.3 GPa can now be routinely made. This is equivalent to a buckle pressure greater than 2.0 psi for a 1 μm thick, 900 μm diameter shell. This value is comparable to those quoted for vapor deposited polyimide shells. It is about twice as high as what we make using the GDP deposition conditions used for normal deliveries. The stronger shells are about three times more permeable than normal GDP shells. The combination of higher strength and higher permeability should give a factor of 6 reduction in the time needed to fill a thin-walled shell to high pressure and is ideal for LLE cryogenic experiments. We used our modified process for two deliveries to LLE last year. We have found that the high strength GDP shell material also has higher density than our standard GDP material. The high strength GDP material has a density of about 1.4 g/cc versus 1.1 g/cc for the standard GDP material.

1.10. UR03 OMEGA FLAT FOIL FABRICATION

The NR01 and UR03 tasks are, as in past years, closely related. The production of flat films for both the NIKE laser program at the Naval Research Laboratory (NRL) and the OMEGA laser program at UR/LLE utilizes many of the same techniques. LLE targets are generally not mounted, but delivered as flat foils. This past year the foils have been made of PS or layered PS and silicon-doped polystyrene (Si-PS). The surfaces of the foils have been smooth or patterned.

During the past year, we have directed a great deal of effort toward improving the quality of the foils we send LLE. Principally, our efforts have gone toward making a better-defined boundary between heterogeneous layers in the foils. By experimenting

with various solvents, materials, and casting techniques, we have reduced mixing at the layer interface and have reduced cracking and deformation of the layers.

1.11. CR/LL1 ENHANCED CRYOGENIC TARGET FIELDING DEVELOPMENT

The goal of the national cryogenic target program is to prepare the necessary technology and infrastructure in time for the scheduled cryogenic target campaign on the NIF. Task CR/LL1 provided two scientists and one technician to LLNL to support the development of cryogenic targets and cryogenic target systems. The GA/Schafer team is an integral part of the LLNL cryogenics team and all of our reported efforts have involved close collaboration with LLNL personnel.

A large portion of our effort has gone into optimizing D-T ice fuel layer growth techniques. A study was completed on the possibility of slowly cooling a perfectly formed layer of D-T from just below the final freezing temperature, (~19.7 K) to 18.2 K. Even very smooth layers roughen significantly when cooled below about 19.5 K. It was concluded that this is not a viable technique for beta layered targets.

Further study was made of techniques to create a perfect D-T layer at 19.7 K. Initial orientation of the seed crystal with respect to the plastic capsule surface has a large effect on the final layer smoothness. Capsule fill tubes act as a natural site for formation of this seed crystal. It will be important to try and control this crystal orientation effect as experiments on permeation filled shells begin.

Very good news has been produced in the infrared (IR) enhanced layering experiment. This technique simulates beta layering by exciting collisionally induced rotational-vibrational transitions in hydrogen isotopes. With a new IR laser, layering experiments using hydrogen-deuterium (H-D) have been conducted that generated bulk heating rates of up to 40 times that occurring due to the natural beta decay in D-T. At the higher powers we have been able to take smooth layers created just below the triple point of H-D and cool them to 1.5 K without any significant degradation.

Current work is in progress to replicate this result with D-T. Possible complications are the existence of IR adsorption lines at wave length 2.7 to 4.0 μm in current plastic capsules that overlap the D-T IR resonances and may interfere with the enhanced layering process.

Development of a new experiment to develop IR illumination techniques in hohlraums took place in the past year. Design and assembly has been completed. Results will be forthcoming early next fiscal year.

The D_2 Test System being built by GA is scheduled for delivery in the second quarter of FY01. Part of the CR/LL1 effort has been to help prepare the necessary infrastructure

for the new system. Contributions have included optical design and layout, safety interlock requirements, and high pressure fill system design.

1.12. CR/LL2 NIF CRYOGENIC TARGET SYSTEM DEVELOPMENT

The deuterium test system (D_2TS) is designed to allow layering and other experiments on full-sized, fully filled indirect drive target assemblies, where the target's capsule does not have a fill-tube attached. The capsule is permeation filled to high deuterium density. The D_2TS consists of eight main subsystems (Fig. 1.12–1): the main cryostat, the cryogenic target gripper, the permeation cell, the permeation cell housing and motion system (PCHMS), the permeation cell cooling and support system (PCSCS), the permeation cell plug remover (PCPR), the cryostat sliding mount, and the gate valves. During FY99, the D_2TS design was improved for better operability, better integration into the laboratory location (which was decided this year), and for ease of LLNL Safety Committee approval. Fabrication and procurement were started for all of the major subsystems except for the PCSCS. The PCSCS design drawings were nearly completed.

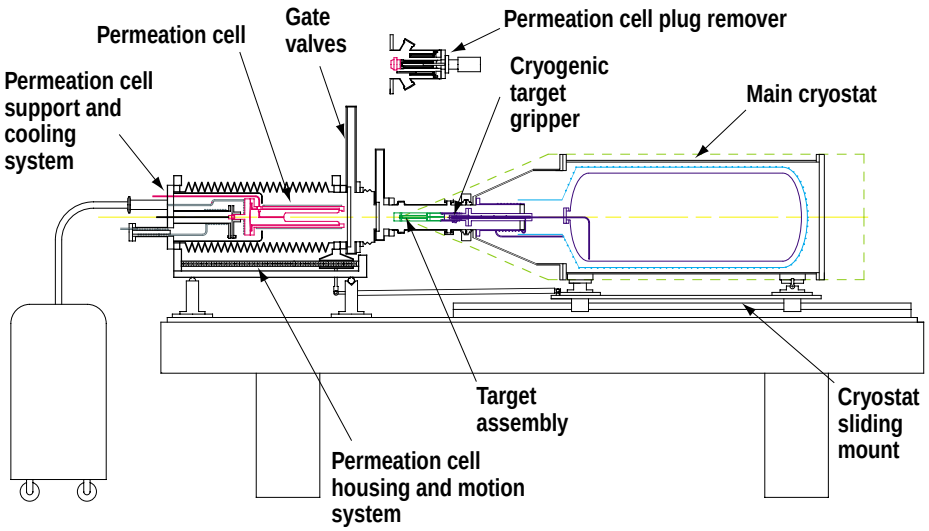

Fig. 1.12–1. The main cryostat of the D_2TS retrieves a target assembly from the permeation cell once the target has been filled and cooled.

The cryogenic target gripper was fabricated; a test fixture was built; and the gripper tested for thermal, electrical, mechanical, and gas sealing performance. The gripper successfully met the performance goals set for it. We expect to complete the assembly, testing, and installation of the D_2TS at LLNL next year.

Concepts for the NIF cryogenic target system (NCTS) were further examined. The "1A" concept for the NCTS was looked at and altered to handle direct drive targets. The

strengths and weaknesses of the "1A" type concept and the French concept for the Laser Megajoules (LMJ) Cryogenic Target System (CTS) were investigated. A large number of hybrid concepts between the NCTS and LCTS were developed. The goal was to look for concepts that could be used at both NIF and LMJ with the system at each site being the same or only slightly modified.

1.13. CR/LA1 BETA LAYERING SUPPORT AT LANL

Beta-layering work at LANL during FY00 included the completion of several tasks concerning the design, installation, and testing of various elements of the cryogenic pressure loader (CPL) system. Additionally, a new series of solid layering experiments were begun in order to examine the effects of D-T aging in a beryllium torus having the same surface/volume ratio as a sphere. FY00 work also included the performance of detailed image analyses on a D-T solid layer inside a LLNL 2-mm sphere.

The CPL system consists of a cryostat with integrated permeation cell, layering sphere, and target insertion mechanism. This system will have the capability to permeation-fill NIF-sized capsules with D-T to pressures as high as 1500 atm. It will be used to test D-T target filling and solid layering operations, as well as measuring the amount of D-T release from the target filling permeation cell to the cryostat volume. The apparatus will also demonstrate the ability to produce β-layered targets as well as perform optical target characterization. The CPL system also includes an optical system external to the cryostat, and an interlocking hardware and software interface between the facility instrumentation and control system (ICS) and the CPL control system

The CPL control system will control target insertion and layering sphere positioning mechanisms, as well as the x-y-z stage positioning mechanisms for the image acquisition and real-time monitoring cameras and optics. The CPL optical system functions as an image acquisition system and monitor for the target capsule, once it has been filled in the permeation cell and lowered to the D-T layering sphere position. The image acquisition and monitoring systems will acquire and save images of the solid layering process, as well as provide on-going monitoring of the process in real-time.

The CPL-ICS interface is an interlocking interface between the CPL control system and the WETF ICS and has been designed to fulfill the tritium operations engineering requirements at the WETF. This system will allow the WETF facility operator (FO) to enable or disable certain D-T gas handling operations by the CPL control system and will provide CPL status information to the FO.

During FY00, detailed surface roughness measurements were performed on a D-T solid layer inside a 2-mm sphere using two different techniques. The images were acquired during an experiment done at LLNL in which the layer was produced by a

slow-freeze process and analyzed at LLNL using their new Gaussian Fit algorithm. We performed detailed edge trace analyses of the "white band" image of the inner ice surface using our standard nonlinear fit (error function) routine. We analyzed the inside and outside white band edges as well as the outside of the 2-mm sphere, and got close agreement over the critical middle modes ($\sim l$ = 3 to 30) [see Fig. 5.2–4(b)] between the outside edge measurement and the LLNL Gaussian fit for modes 2–30.

1.14. CR/UR1 OMEGA CRYOGENIC TARGET SYSTEM ENGINEERING

All OMEGA Cryogenic Target System (OCTS) equipment was delivered to UR/LLE in FY99. The workscope in FY00 consisted of preparation of project closeout documentation and consulting support.

Consulting and response to inquires were provided as requested by UR/LLE. A report documenting the cryogenic tests performed on the moving cryostat at GA was completed (GA memo ICFT99/257). K. Boline attended the 13th Target Fabrication Meeting, and presented a poster, "Cryogenic Testing of a Mobile Cryostat for OMEGA." The last deliverable item was the stress report for the cooldown of the FTS dome. This document, "Cooldown Transient Calculations for Upper Dome of the OMEGA Project Fill/Transfer Station (FTS) Cryostat," (GA memo 660:CMC:001:00) was delivered to UR/LLE in April.

2. COMPOSITE POLYMER CAPSULE DEVELOPMENT AND PRODUCTION

Although the delivery of capsules, targets, and samples are our prime and highest priority activity, incremental development of new and improved techniques are critical for keeping the U.S. Inertial Confinement Fusion (ICF) program supplied with the highest quality and the greatest range of well-characterized components at reasonable cost. We report improvements in making poly(α-methylstyrene) (PAMS) shell mandrels, glass shells, glow discharge polymer (GDP) shells, poly(vinylalcohol) (PVA) deposition, and characterization techniques.

PAMS shells are critical for current target production and are likely to also be critical for future National Ignition Facility (NIF) targets. Over the last two years with Lawrence Livermore National Laboratory's (LLNL) Masaru Takagi working onsite at GA, excellent synergy between LLNL and GA has led to significant development. This year, Takagi's introduction of polyacrylic acid in the outer water solution (W2) of the microencapsulation process greatly improved sphericity (power modes 2 and 3) and Barry McQuillan's control of Marangoni convection greatly improved the mode 10 problem (low modes between 8 and 30). Due to these two discoveries, both NIF scale PAMS and the smaller diameter PAMS required for current experiments have been improved.

New developments in glass shells lie in Martin Hoppe's continued development of his discovery of pyrolyzing silicon-doped glow discharge polymer (Si-GDP)shells into glass shells. This technique has greatly extended the large diameter, thick-walled sizes available for the ICF program. Related to this, Hoppe found that the surface finish of GDP-coated glass shells can be improved by a thin coating of polystyrene (PS).

Omega's cryogenic experiments require a 950 μm diameter polymer shells with walls as thin as 1 μm. The shells must be strong and highly permeable so that filling them with high pressure deuterium-tritium (D-T) can be completed in a reasonable period of time. For the past two years, Abbas Nikroo has led the development by determining the relationship between coating parameters and the strength of thin GDP shells. Nikroo found that lowering the pressure in the coater was the key, making GDP shells that approach the strength and permeability of the other candidate material, polyimide. The surface finish of the GDP shells is much better than polyimide. Furthermore, the density of the high strength GDP is much higher than normal GDP, 1.40 g/cm^3 versus 1.04 g/cm^3, and is close to the density of polyimide. For NIF capsules, higher density is expected to improve performance. Thus, this high strength GDP may be a good candidate for use in NIF capsules.

PVA coating of Nova scale (0.5 mm diameter) capsules has been called the "Vietnam of target fabrication" (Bob Cook, LLNL) due to the historically low yield of the process in spite of over a decade of development. Generally, only about 2% of the shells coated with PVA are of target quality. Wes Baugh modified our coating apparatus and the increased yield to 17% in initial experiments. The modification was made at the end of the year. Additional development in FY01 will determine if the greatly improved yield is reproducible. Larger diameter shells must be coated by another technique. David Steinman is developing dip coating and alternative techniques.

Over the last several years, characterizing surface finish has become required for more and more capsules. The measurement of wall thickness variations is beginning to be requested for a significant number of targets. The Spheremapper and the Wallmapper are the devices used for the measurements. Richard Stephens and Lloyd Brown led the effort to upgrade both, increasing the range and productivity. Martin Hoppe built a device that accurately determines the pressure or permeability of filled capsules. In addition, Stephens discovered that polarized light can be used to rapidly examine the entire capsule for surface anomalies.

2.1. PAMS SHELLS

An inner PAMS shell serves as the mandrel upon which the GDP is deposited. It is the heart of the capsule fabrication process. We investigated several techniques to improve the quality of our PAMS shells in FY00.

2.1.1. Mode 10 Improvement

PAMS shells made in previous years on the dual orifice droplet generator had one very characteristic defect — a "mode 10" problem [Fig. 2.1–1(a)]. Shells which were spheremapped, showed a lumpiness, with about 10 lumps around the circumference of OMEGA shells (mode 10), and about 17 lumps around a NIF 2-mm shell (mode 17). The amplitude of this lumpiness was larger than the NIF standard curve specified. Such lumps in the PAMS mandrel would be replicated in the final target, and would be an unacceptable source of Rayleigh-Taylor instability upon compression.

This year, it was proposed that the source of this nonuniformity is Marangoni convection in the wet polymer/solvent system, driven by the concentration gradient as the solvent is being removed from the shell during curing [2–1]. Marangoni convection is typically seen only in thin films, less than about 500 μm thick. (In thicker films, the analogous Rayleigh convection dominates the convection.) In most Marangoni convection studies, heat transport across flat films leads to surface tension gradients, the combination of which leads to convection cells. In our case, mass transport of solvent

(fluorobenzene) across the polymer/solvent (O1) spherical shell leads to interfacial surface tension gradients on the exterior surface of the shell. Once the demand for removal of fluorobenzene is greater than diffusion of fluorobenzene can supply to the surface, convection cells are formed to supply fluorobenzene faster. The convection cells also bring polymer to the surface and the polymer builds up as lumps on the surface, and these lumps remain on the dry shell surface.

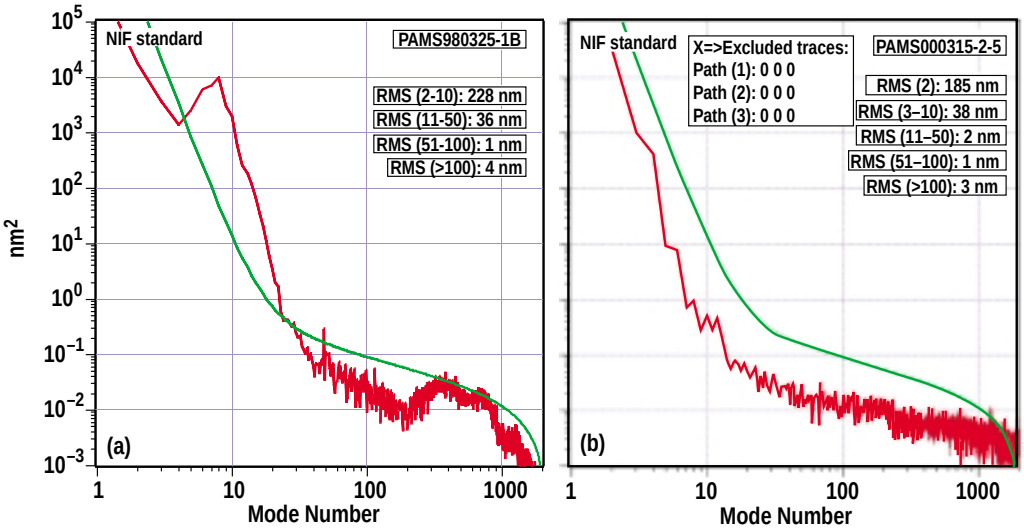

Fig. 2.1–1. Comparison of PAMS shells (a) with mode 10 > NIF specification (b) mode 10 < NIF specification.

A theoretical model of Marangoni convection in spherical shells was used to predict and compare with our shell data [2–2]. We were able to correctly calculate the mode to be expected in OMEGA shells was mode 9–10. In 2-mm NIF shells, mode 17 was correctly predicted. These correlations gave support to the contention that the "mode 10" defect was related to Marangoni convection. Calculations of the model also showed that, to a first approximation, the observed convection cell size along the surface is roughly four times the O1 thickness, thus giving us a simple estimate of what mode number would occur for a given wet shell.

Convection cells are formed when a particular combination of wet shell parameters exceed a critical value (unitless), called the critical Marangoni number

$$M = [(d\gamma/dC)\,(\Delta C)\,(\Delta R)]/(\eta\, D) > M_c \quad ,$$

where $d\gamma/dC$ is the gradient of surface tension with concentration along the exterior surface of the shell, ΔC is the concentration gradient of fluorobenzene across the O1 shell during the removal of solvent, ΔR is the thickness of the O1 wall, η is the viscosity of the O1 wall, and D is the mass diffusivity of the fluorobenzene in the O1.

This theory was developed for a static layer where none of the parameters change with time. In the case of these shells, as the shells cure, the O1 concentration changes, and all the parameters in the Marangoni number also change: ΔR gets smaller, η gets larger, and D and $d\gamma/dC$ change in an undetermined way. Looking only at the ΔR and η, the Marangoni number decreases as the shells cure. The observed mode structure correlated with the ΔR of the initially formed wet shell. ΔR dramatically changes from 122 to 18 μm during the curing, but the 122 μm starting O1 thickness predicts the correct mode structure, and the observed final mode structure does not seem to change as ΔR shrinks.

With this understanding, we could look at the Marangoni number for ways to eliminate the convection cells in our process. First, if ΔC, the concentration gradient across the O1, is decreased sufficiently, one may reduce $M < M_C$. ΔC can be reduced by slowing the removal of fluorobenzene and thereby slowing the curing time. Takagi (LLNL) slowed the curing time for NIF shells from 1 day to 4 days by flowing fluorobenzene vapor over the curing shell solution surface and thereby removed the lumpiness on the surface of NIF shells.

A second way to reduce convection in OMEGA shells was using an indirect reduction of ΔR. A starting solution of 11% PAMS in fluorobenzene had been the reference O1 solution, and it lead to shells with 18 μm final walls and significant “mode 10”. By reducing the O1 to 8%, and making shells with the same initial O1 thickness, shells with a final wall thickness of 12 to 13 μm were made without the significant “mode 10”. In effect, by starting at 8%, there had to be convection cells at the start of the wet shell curing just like in the reference 11%, but by the time the shell reached 11% in polymer concentration, ΔR is then smaller (89 μm) than the ΔR of the reference process (122 μm). At this point, the value of M for the starting 8% O1 is roughly 72% of the value of the Marangoni number of the reference shell made from 11%. At the 11% O1 in the new shell, the new shell is closer to shutting off convection (if it has not yet shut off) than the reference shell. By starting with the 8% O1, the convection shuts off sooner at a lower PAMS concentration, where the solution still has a small enough viscosity for the polymer lumps to diffuse back into the wall before the shell hardens. Thus, the mode 10 lumpiness is reduced in these OMEGA shells, by a combination of smaller ΔR and smaller viscosity, with the Marangoni number falling below M_C at a smaller O1 viscosity. Figure 2.1–1(b) shows a representative power spectrum without mode 10. Figure 2.1–2 shows that for an 8% O1, shells below 14 μm wall thickness all have a much reduced mode 10 amplitude — some 100 to 1000 fold smaller than for an 11% solution.

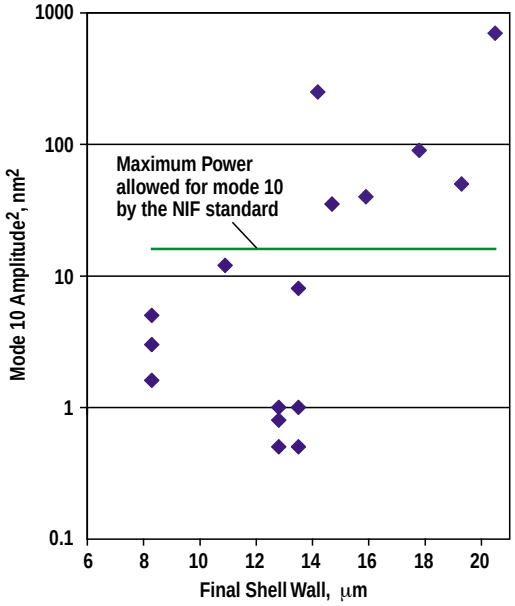

Fig. 2.1–2. Amplitude at mode 10 for OMEGA shells of various final dry wall thicknesses, for a starting 8% PAMS in fluorobenzene O1 solution. Shells with walls below 14 μm show a much reduced mode 10 defect, implying that convection cells turned off at solution concentration where viscosity is low enough for lumps to flow into a smooth surface. Line at ~20 nm^2 is the NIF specification value for mode 10.

2.1.2. Use of PAA to Reduce OOR

Takagi (LLNL) showed last year that replacing PVA in the W2 with polyacrylic acid (PAA) decreased the out-of-round (OOR) for 2-mm NIF shells. In making the above OMEGA shells in a PVA W2 solution using the new 8% O1 solution to reduce the mode 10 problem, the OOR of the shells increased above the 1.0 μm specification. We reduced the OOR below 1.0 μm, by using PAA (0.01 wt% of MW = 1,00,000; PVA 0.3 wt%, MW 25 K), but only by removing the use of salt (NH_4Cl) in the W2. Apparently, NH_4Cl cancels the increased interfacial surface tension effect of PAA. The removal of NH_4Cl leads to the reappearance of multiple vacuoles. These many small vacuoles seem to not be a problem at the surface of the PAMS as they do not show up in the high mode structure on the spheremapper.

The combination of PVA and PAA appears to also decrease the high mode surface debris which seems characteristic of shells made using only PAA. OMEGA shells made with PVA and a combination of PVA and PAA almost always show spheremapper amplitudes near 1–3Å over modes 100 through 1000. NIF shells, made with pure PAA, show higher spheremapper amplitudes (10 to 50Å) over the same modes. Preliminary

work by Takagi adding some PVA to the PAA W2 solution during the curing phase shows some reduction in these high mode amplitudes.

2.2. GLASS SHELLS FROM DOPED GDP

We discovered in 1998 that it was possible to make high quality glass shells by adding another step to the GDP/PAMS process [2–3,2–4]. In step one, doped GDP is deposited on PAMS shells. The dopant needs to be one that forms a suitable oxide, such as silicon or titanium. In step two, the shell is pyrolyzed at about 300°C in an inert gas, such as nitrogen, to remove the PAMS. In the final step, the doped GDP shell is pyrolyzed in an oxygen-containing atmosphere to convert it into a glass shell (Fig. 2.2–1).

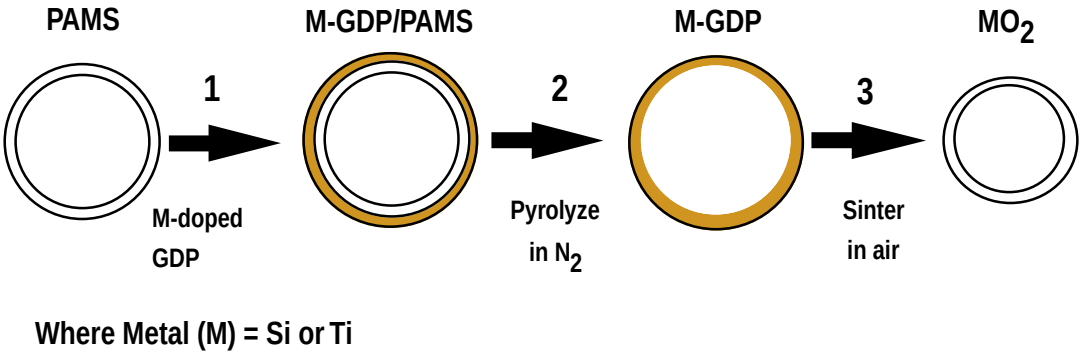

Fig. 2.2–1. Doped GDP shells are converted to glass shells.

Utilizing this process we delivered glass shells this year with diameters of ~260 µm and ~23 µm walls; ~900 µm and ~3.8 µm walls; and 1450 µm and ~14 µm walls. An example of the wall uniformity of thick walled glass shells that were delivered to the labs by this process is shown in Fig. 2.2–2.

The plot shown below (Fig. 2.2–3) compares the range in diameters and wall thicknesses of glass shells which have been made by the drop tower method and by the Si-GDP route.

Previous to this year, the largest high quality PAMS mandrels we had available for this project were near 2100 µm in o.d. with ~12 µm walls. Due to the substantial shrinkage (~30 % in o.d. and wall) that occurs in the sintering step of the process the largest glass shell one could make would be near 1400 µm o.d.

This year, thanks to efforts of Dr. M. Takagi, PAMS shells ~3.2 mm in size were made. During the few times the GDP coater was not being used for an official lab order coating, runs were made in attempts to make glass shells as large as 2 mm in diameter.

Although, with some effort we succeeded in successfully making free-standing ~3.4 mm Si-GDP shells (Fig. 2.2–4), we were unsuccessful in converting any of them into an intact glass shell.

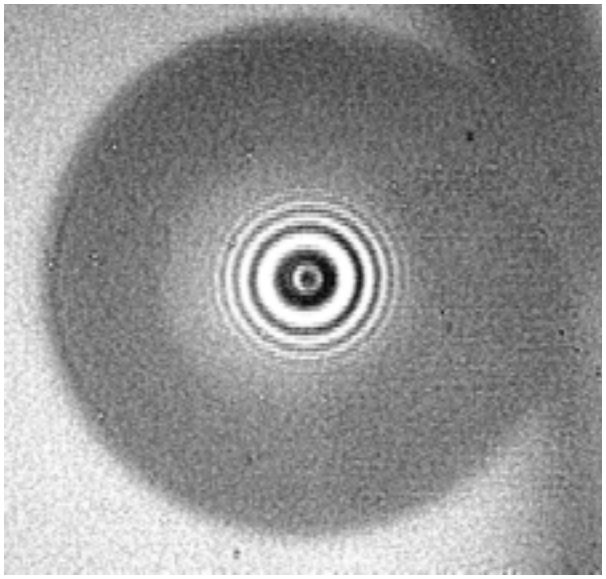

Fig. 2.2–2. The fringe pattern of a ~280 µm o.d. x 22 µm wall glass shell produced by the Si-GDP method illustrates the excellent wall uniformity that can be made by this process.

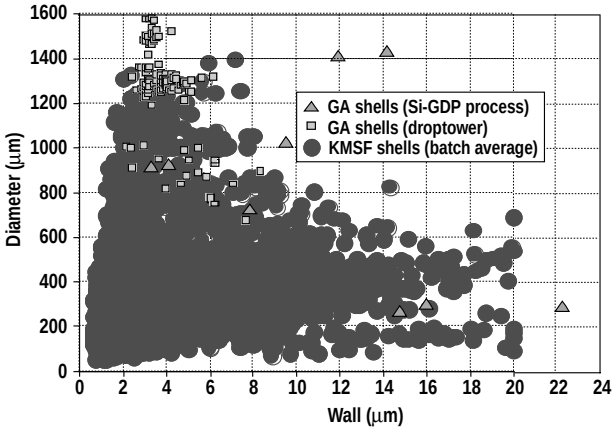

Fig. 2.2–3. The range in o.d. and wall thickness of glass shells made over the years by the high temperature drop-tower method and by the new Si-GDP method are shown. The Si-GDP method gives us access to shell sizes not possible to date by the drop-tower route.

It appears that large debris-like features embedded into the Si-GDP increase the difficulty in converting the Si-GDP into glass. These features perhaps generate stress

points during the pyrolysis conversion process that results in the shell fracturing into large shards. In one instance when the shell broke into two large hemishells during the conversion process, the fracture line ran directly into one of these features and the nodule actually popped out and left a small hole bisected by the fracture line. The intact nodule feature was found in the bottom of the pyrolysis boat.

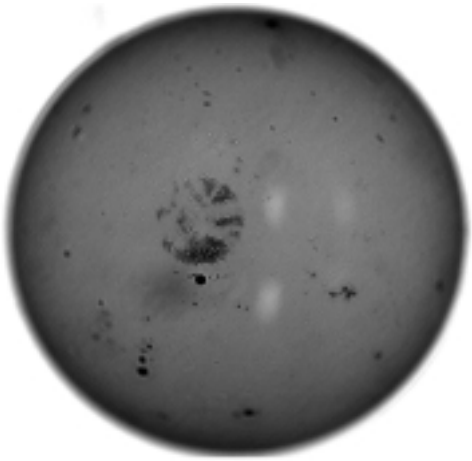

Fig. 2.2–4. Surface picture of a 3385 µm o.d. x 25.6 µm wall Si-GDP shell. Due to the PAMS mandrel quality, there are numerous surface inclusions evident.

Masa Takagi has resumed efforts to make additional >3 mm PAMS shells which have much fewer inclusions within the PAMS walls that lead to large defects in the resulting Si-GDP coating. Once these PAMS mandrels become available and we have coater time, we will attempt again to make ~2 mm glass shells via this process.

In addition to attempting to make 2 mm o.d. glass shells, we also provided D-GDP coated glass shells to LLNL for infrared (IR) layering experiments. The surface finish of the vapor deposited D-GDP overcoat proved to be too rough for the interferometry measurements. Glass shells made by the Si-GDP process tend to have a rougher background surface finish in the high order modes (>100) than drop-tower produced shells. During deposition of the D-GDP, the surface roughness was magnified to the point that interferometric measurements in the system at LLNL were not possible. Figure 2.2–5 compares the typical surface finish of the bare glass mandrels to that after deposition of the thick D-GDP overcoat.

In efforts to smooth out the high order mode roughness of the D-GDP overcoat, we first applied a layer of PVA by the dip-coating technique. This resulted in a significantly smoother surface finish in the high mode spectrum but interferometric tests showed that it still was not smooth enough. We then tried overcoating a D-GDP coated shell with PS by the dip-coat technique followed by vapor smoothing with Toluene. This resulted in an

even smoother surface finish. Interferometric results on the capsule are not yet complete. Figure 2.2–6 compares the smoothing improvement of the PVA and vapor smoothed PS as measured by the spheremapper atomic force microscope (AFM).

For additional information contact Dr. M. Hoppe (GA).

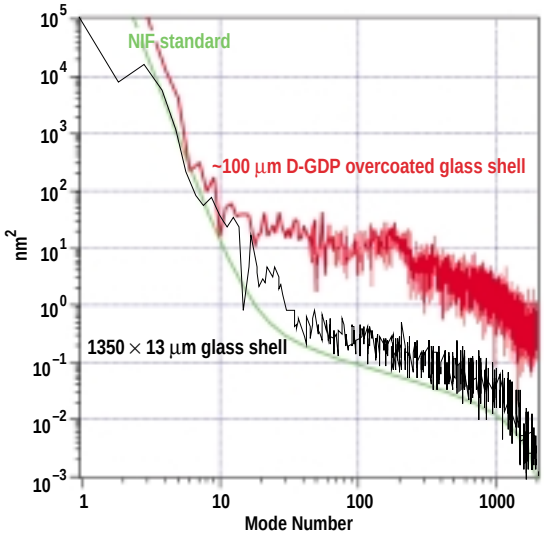

Fig. 2.2–5. The already somewhat rough high order modes on the glass shell made by the Si-GDP process became much rougher after D-GDP coating.

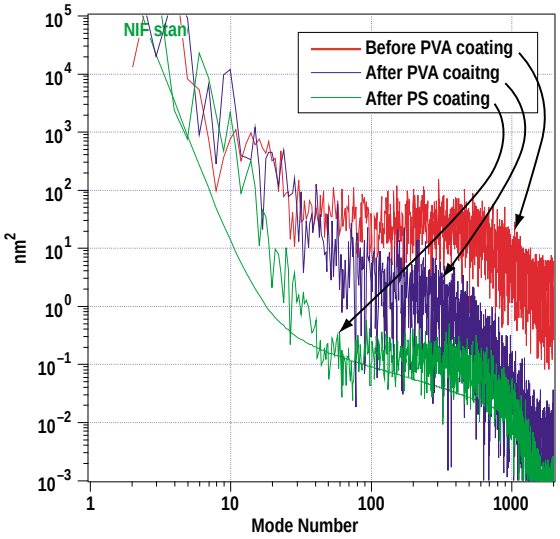

Fig. 2.2–6. Vapor smoothing of the PS layer after the dipcoating process resulted in capsules that were superior in surface finish than those dipcoated in PVA with no vapor smoothing.

2.3. STRONGER, DENSER GDP SHELLS

Thin walled polymer shells are needed for OMEGA cryogenic laser experiments. The capsules need to be about 900 μm in diameter and as thin as possible (≈1 μm) while having enough strength to be filled with D-T as fast as possible to about 1000 atm. This requires that these high aspect ratio shells have high buckle strength and permeability. Last year we began to investigate the strength of the GDP shells we normally fabricate using the PAMS/GDP process and the possibility of strengthening them by changing the coating parameters [2–5]. We continued this work in FY00.

The theoretical buckle strength of an ideal defect-free spherical shell of wall thickness w and diameter D, is given by [2–6],

$$P_b = E\left(\frac{w}{D}\right)^2 \frac{8}{\sqrt{3\left(\nu^2 - 1\right)}} \quad ,$$

where E and ν are the Young's Modulus and Poisson's ratio for the material, respectively. Therefore, to perform a comparison of buckle strength of shells made under different conditions, any difference in the aspect ratio, D/w, needs to be properly accounted for. We have done this by calculating the Young's Modulus and using this value when comparing the strength of different batches of shells. ν was assumed to be 0.30, typical for polymers. We and others have tested the validity of this procedure [2–5,2–7] for wall thicknesses greater than ≈1 μm. From the above, it is clear that three different quantities need to be measured for each shell. Namely, the wall thickness, diameter, and the buckle pressure.

The buckle pressure was measured using the device we built last year. Briefly, a prechamber is pressurized to the desired test pressure. The shells are then subjected to this pressure in less than 1 s to avoid filling the shells as they are tested. An attached camera allows observation of shell buckling directly. This device was upgraded in FY00, including the addition of a fine control regulator capable of reaching 50 psi in 0.1 psi steps. We estimate an error of <3% for buckle pressure measurements. Shell diameters were measured using the standard characterization techniques used in our laboratory. The diameter could be measured to ≲1 μm, resulting in an error of <1% when measuring 900 μm shells. Using interferometry, we normally measure shell wall thickness to about 0.1 μm. For a 1 μm thick shell, this translates into a 10% error which propagates into a 20% error in the Young's Modulus. This represents the largest error in determining the Young's Modulus. To verify the wall thickness values found by interferometry, we also used destructive scanning electron microscope (SEM) measurements for many of the

batches. The comparison is shown in Fig. 2.3–1. The agreement was to about 0.1 μm (<10%) for almost all batches.

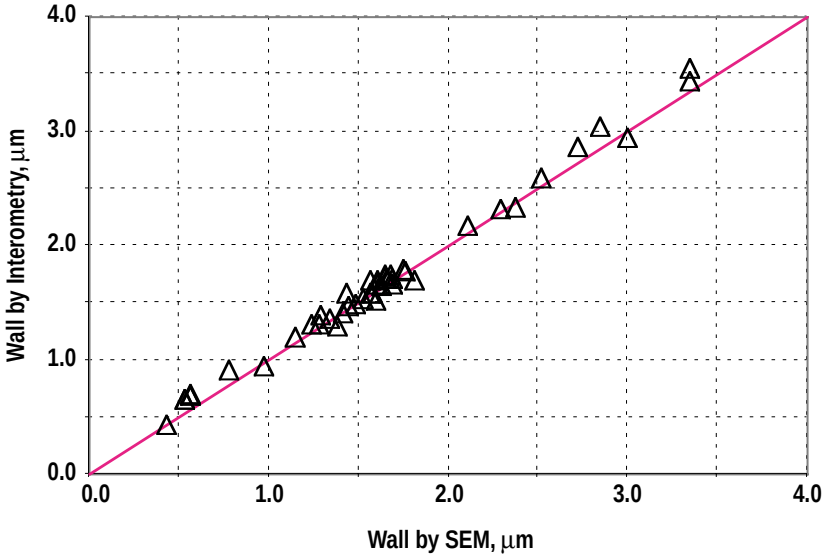

Fig. 2.3–1. Comparison of wall thickness measurements by interferometry and SEM. SEM measurements were used to verify values obtained by interferometry.

Initially, we performed a number of runs to confirm our results from FY99 regarding the effect of coating pressure on the buckle strengths of thin-walled GDP shells. Each run was duplicated three times to examine run-to-run reproducibility as well. The duration of pyrolysis was kept fixed at 8 h. This pyrolysis procedure was used in almost all of the experiments described in this section. To study the variability, 15 to 30 shells from each batch were buckle-tested. These runs confirmed that with all other parameters constant, coatings made at lower pressure lead to stronger shells. We then began to examine some of the other parameters involved in making GDP shells via the PAMS/GDP process.

2.3.1. Coating Gases

We studied the effect of gas flow ratios in the GDP process. We performed a number of runs varying the hydrogen (H_2) to trans-2-butene (T2B) flow ratio. The coatings were performed at 20, 25, 40 and 75 mtorr. At first, the H_2 flow was kept constant at 2.0 sccm while the T2B flow was varied between 0.08 and 0.32 sccm. The H_2/T2B ratio had a dramatic effect on the strength of the shells, especially at the lowest pressures (Fig. 2.3–2). The higher H_2/T2B flow ratio resulted in higher strength shells. The effect was more pronounced at 20 and 25 mtorr. Using optimized flow ratio we could routinely make ≈1 μm shells with Young's Modulus of over 2.3 GPa. This is comparable to Young's Modulus values reported for vapor deposited thin walled polyimide shells [2–8].

In practical terms, this translates into a buckle pressure of 2.0 psi for a 1 µm thick, 900 µm diameter shell. Batches with Young's Modulus values of over 3.0 GPa were also made at times. GDP run-to-run variation is the most likely cause of variations in the observed Young's Modulus values.

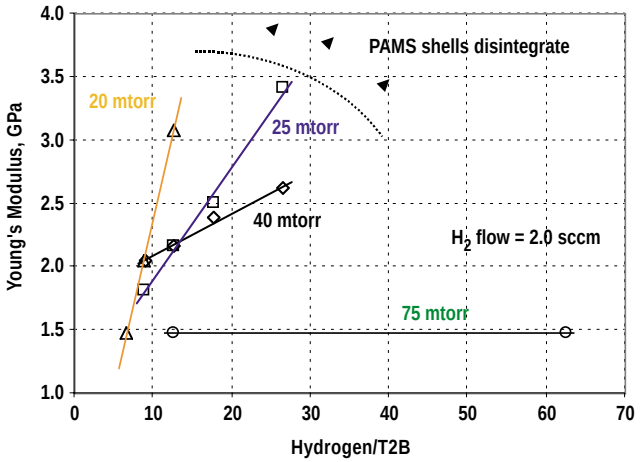

Fig. 2.3–2. The hydrogen-to-T2B flow ratio used in the GDP coating had a dramatic effect on the strength of the final GDP shells. This was true only for the lowest deposition pressures where the strongest shells are usually made. PAMS shells disintegrated for flow ratios above a certain point possibly due to hydrogen etching and lack of hydrocarbon species.

The surface finish also improved as the T2B flow was decreased at constant H_2 flow (Fig. 2.3–3). The surface finish improvement with increasing H_2/T2B flow ratio is well known in our GDP deposition system and had been previously attributed to the lowering of T2B residence time. However, in this case, the constant H_2 flow results in constant T2B residence time due to the much higher H_2 flow. Therefore, the etching effect of H_2 is the most likely cause of the simultaneous surface finish improvement and higher strength of the films. The amount of diameter shrinkage in the pyrolysis also decreased with increasing H_2/T2B flow ratio. At the highest H_2/T2B ratios and at 20 and 25 mtorr coating pressures, the PAMS shells disintegrated rapidly (Fig. 2.3–2). This is probably due to the lack of sufficient hydrocarbon precursor in the coater to form a coating and the resulting hydrogen etching of the PAMS shells.

We also explored higher H_2 flows at constant, rather high (0.16 sccm), T2B flow and observed the same effect. However, in this case, at the much higher H_2/T2B flows, the PAMS shells did not disintegrate. Apparently, the T2B flow was high enough to obtain a coating despite the high H_2 flow; however, the resulting shells were weaker in this regime. The runs involving the higher H_2 flow had the added benefit that the coating on the inside of the plasma tube appeared to be more stable and did not flake onto the shells during the run. This flaking is a common problem for runs at low pressures and low H_2

and T2B flows. The absence of such flaking in the higher H_2 runs allowed longer runs to make thicker shells (>2 μm) if needed without multiple tube changes during the run. This proved to be very useful in the case of a delivery to University of Rochester/Laboratory for Laser Energetics (UR/LLE) where 3 μm thick shells were requested.

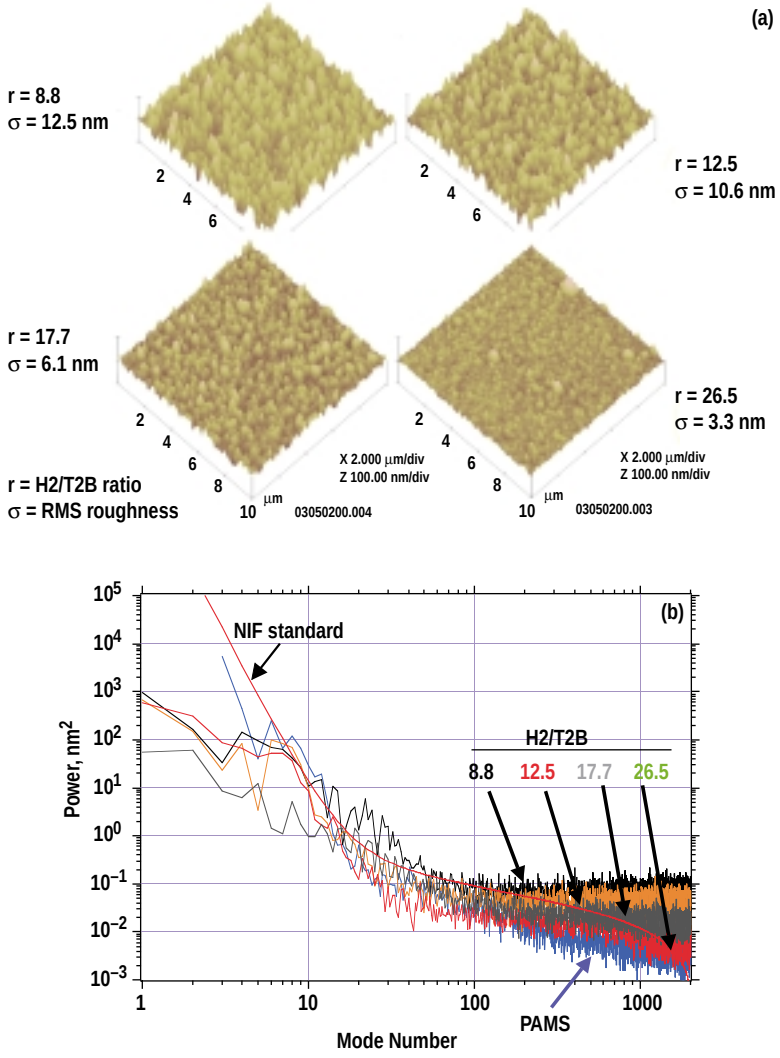

Fig. 2.3–3. (a) Atomic force microscope patch scans of surfaces of ≈2 μm GDP shells. The higher hydrogen-to-T2B ratio results in smoother surfaces. These coatings were deposited at 40 mtorr. (b) AFM spheremaps of the shells shown in (a). The low mode power (<100) is mainly due to the starting PAMS shell. The higher mode power (>100) is dominated by the hydrogen to T2B flow ratio as shown (a) also. The bare PAMS shell spectrum is also shown for comparison.

We investigated replacing T2B, the usual hydrocarbon precursor used for GDP coatings, with first methane and then benzene. As with T2B, we were able to make shells with Young's Modulus over 2.3 GPa with these precursors. The coating parameters had to be optimized in each case. The strongest shells made using methane were 10% to 20%

weaker than the strongest shells made using T2B. Relative hydrogen flow had a large effect on the strength of shells made using methane similar to what was observed for T2B. For benzene, while there appears to be a similar trend, the results are not as reproducible. A recent run, using benzene, produced shells with Young's Modulus over 4.0 GPa, the highest value obtained to date. However, other runs using identical parameters resulted in shells with much lower moduli. Coatings involving benzene have been much less studied than the other two precursors. We hope to investigate benzene as a precursor more thoroughly in the future.

A major goal of seeking stronger shells is to allow thin-walled shells to be permeation filled more quickly. A major concern, therefore, was whether the stronger GDP shells might have lower permeability. Numerous permeability measurements of the shells made using T2B against various gases such He, Ne, N_2 and Xe indicate that the reverse is true (Fig. 2.3–4). Measurements for He, Ne and N_2 were made destructively using buckle strengths measured for the batch. Xe permeability was measured using x-ray fluorescence (XRF). The stronger GDP shells were found to be about three times more permeable than normal GDP shells. We sent Roger Gram at UR/LLE a number of shells from various batches for both buckle strength and permeability measurements. He found that the high modulus shells were three times more permeable to N_2 and Ar and confirmed our buckle strength data. This was an important independent verification of our measurements. D_2 permeability still needs to be measured for these shells.

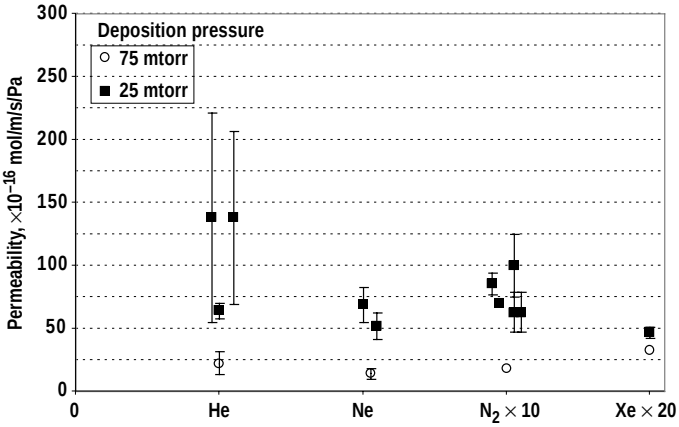

Fig. 2.3–4. The stronger shells made at the lower deposition pressures were more permeable to a number of different gases. The higher permeability is highly desirable and allows filling shells faster.

We determined the chemical composition of our films using combustion analysis. The carbon-to-hydrogen ratio in the high modulus films is about 1.16 while for normal GDP (lower modulus) it is only 0.85. The lower hydrogen content may explain the higher modulus of films made under modified conditions. The oxygen content of the higher

modulus films was also higher (5.5 atomic %) compared to normal GDP (3.0 atomic %). The density of the higher modulus films was measured to be 1.40 g/cc compared to 1.04 g/cc for normal GDP. This is again consistent with the higher carbon content of higher modulus films. This higher density can be of value for indirect drive NIF capsules as well.

2.3.2. Other Parameters

We examined the effects of air or nitrogen storage on the buckle strength of thin GDP shells. This is an important issue, since shells made at General Atomics (GA) will eventually have to be stored for at least a few days at GA and again during shipment before they arrive at OMEGA. A number of different GDP shell batches containing at least 30 shells were made. Each batch was divided equally into four groups. One group was tested immediately. The other three groups were stored under nitrogen for some of the batches and under air for some of the other batches. These groups were subsequently buckle tested after one, two and four weeks of air or nitrogen storage, respectively. The results are shown in Fig. 2.3–5. The data indicates that within the variations seen in each group air or nitrogen storage did not have a significant effect on the buckle strength of GDP shells.

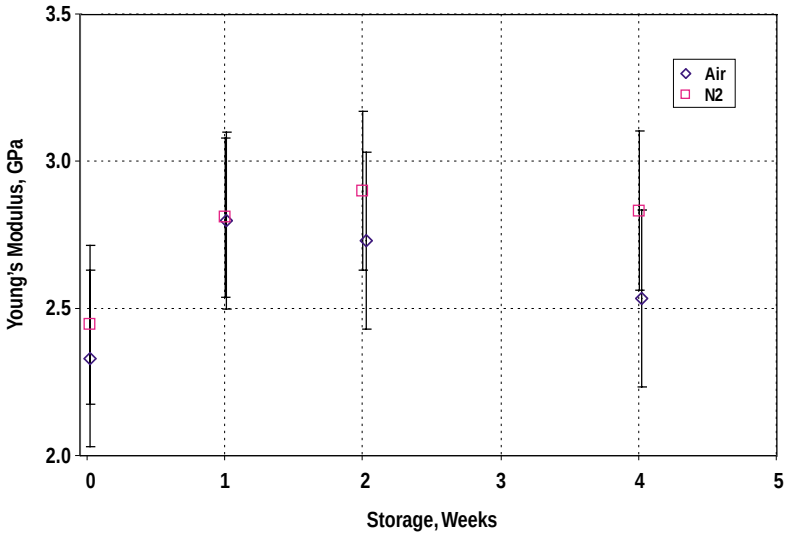

Fig. 2.3–5. Air and nitrogen storage of thin-walled GDP shells was examined. Within the variations observed in the batches used, buckle strength of shells did not change on storage in air or nitrogen over a four-week period.

We also examined the effects of using different PAMS batches on the strength of the final GDP shells. A PAMS batch used in FY99 was used as a control batch in order to account for possible run-to-run variations in the GDP process. Shells from this batch

were coated and pyrolyzed together with shells from the batch which was being tested. This was done with seven different PAMS batches. The results are plotted in Fig. 2.3–6. The most interesting conclusion is that some PAMS batches result in GDP shells with very tight ranges (5% standard deviation) of buckle pressures, while others had much broader ranges (20% standard deviation). In addition, one batch resulted in shells, which were as much as 20% stronger than the control batch we had used in FY99. The tight range of buckle pressures allows testing a small sample of shells from a batch to determine the typical buckle strength for the batch with a high degree of confidence. This leaves the rest of the shells from the batch for other measurements such as permeability.

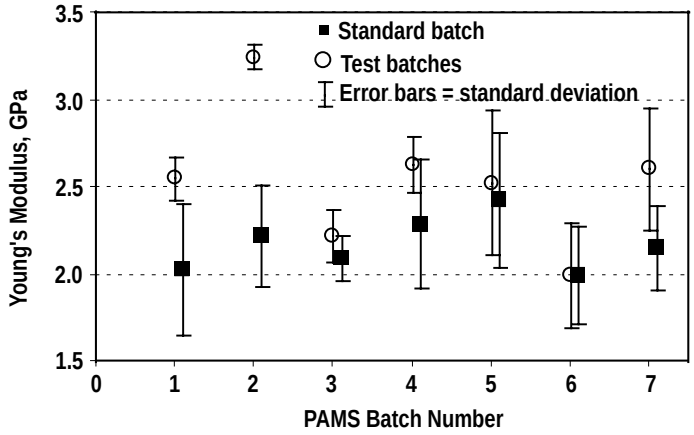

Fig. 2.3–6. The effect of starting PAMS batch on the strength of the final GDP shells was examined. A standard batch was coated and pyrolyzed along with the standard batch which was being tested to account for possible run-to-run variations in GDP coating runs.

We briefly examined some of the other parameters that might affect coating strength. We varied the pyrolysis time. Doubling the pyrolysis time did not affect the strength of shells. We also examined using magnets to confine the coating plasma. The magnet configuration used appeared to result in localized confinement only, which did not benefit shells bouncing over larger areas in the coating pan. Consequently, shells made using this technique did not have as high a modulus as without confinement. Radio frequency (rf) biasing of substrates was also examined. Since our main coating plasma is powered by only 10 W, the biasing field (tens of watts) could create its own secondary plasma. This led to instability in the operation of the coater and the desired bias level. Low bias (≤10 V) levels could be stably sustained, but this did not affect strength of shells. Shells made at higher bias values typically collapsed in the pyrolysis process. A different, slightly modified helical resonator coating plasma head was also used for making high modulus shells. By optimizing the coating parameters, we were again able to make shells with moduli over 2.3 GPa using the second helical resonator. This illustrated the lack of dependence of the process on the particular coating system used.

2.3.3. Conclusion

We have made major advances in developing strong thin-walled GDP capsules. By optimizing the coating parameters, we can achieve a factor of 2 increase in the normalized buckling pressure compared to the usual GDP capsules. This high strength material is three times more permeable than normal GDP to a number of different gases. Shells made from this material can be subjected to twice the pressure and thus permeation should fill about six times faster. The strength of this high-strength GDP is comparable to that of vapor deposited polyimide. The good surface finish that can be achieved with GDP capsules is retained with the high strength material. This material also has higher density (~1.4 g/cc) which may be useful for thick-walled indirect drive capsules. Further optimization and improvement may be possible and should be pursued.

For further information, please contact A. Nikroo (GA).

2.4. PVA COATING IMPROVEMENTS

We improved the PVA drop tower yield of target quality 500 μm capsules from 2% to ~15% by modifying the tower so that capsules would not be lost when injected. We also investigated alternative methods for applying a PVA layer onto 2 mm capsules for Sandia National Laboratory (SNL) experiments on Z.

2.4.1. Drop Tower PVA Coating Improvement

The yield of target quality drop tower PVA-coated capsules at GA has typically been about 2% of the total number of capsules injected into the tower. We surmised that this low yield was affected by the high percentage of shells caught on the walls of the tower entrance tube during their injection into the tower. Wes Baugh found an elegant solution to this problem without resorting to an expensive redesign of the tower. His solution was to lower the shell injection mechanism down into the entrance tube itself. He then devised an observation "peephole" in the tower wall so that the capillary tube could be seen and properly positioned during the shell injection process as shown in Fig. 2.4–1 below.

The PVA drop tower modification described above resulted in a 17% yield of target quality PVA-coated shells in the first production run in which it was employed. It enabled us to deliver capsules to LLNL having a Ti-doped GDP inner mandrel at about a third of the cost of what it would have been without the modification.

2.4.2. PVA Coating of Capsules for SNL's Z-pinch Machine

We investigated several alternative methods of applying a PVA layer onto 2 mm capsules of the type required for SNL's Z-pinch machine. These methods included spraying, dip-and-spin coating, and microencapsulation.

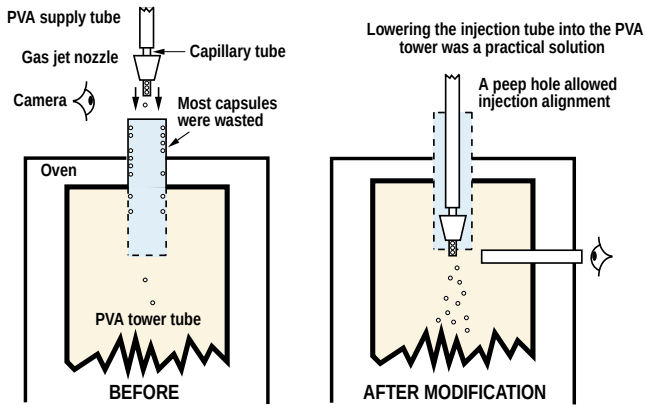

Fig. 2.4–1. The PVA drop tower modification made by Wes Baugh resulted in an increased yield of target quality shells from 2% to 17% in the first production run using Ti-doped GDP mandrels.

As reported in our FY99 ICF Annual Report, our attempts to PVA-coat millimeter size capsules via the drop-tower technique were futile. Due to their large size, the shells fell so fast that the PVA solution covering each shell was still wet at the collection plate at the bottom of the tower. Increasing the tower temperature to its maximum (140°C) did not remedy the problem. Thus, we tried a variety of other approaches.

As previously reported, in FY99 we developed a PVA dip-coating process for millimeter or larger capsules. This process consists of holding the shell with a vacuum chuck and dipping it into an ~7% PVA solution so that about two-thirds of the shell is immersed. The shell is immediately withdrawn from the solution and inverted, so that the PVA will become more uniformly distributed, and allowed to dry for about 10 minutes under a fiber optic light (heat) source. After the shell is dried, it is transferred to a second vacuum chuck that holds the shell at the pole initially dipped in the PVA solution. The shell is then dipped into the PVA solution a second time, the bare half of the shell is coated, and allowed to dry under the fiber optic light source.

A modification of the PVA dip-coating process is to spin the shell immediately after it is dunked into and withdrawn from the PVA solution. The appropriate spin rate should cause the hanging droplet of PVA solution to “spin up” to the shell’s equator due to centrifugal force. We attempted a proof-of-principle experiment to test this concept by rigging up a vacuum chuck assembly to a drill press. We succeeded in redistributing the PVA on the spinning shell but it was obvious from the wobbly nature of the spinning shell that a more elaborate design was needed. We intend to revisit this concept next year if a better way to PVA-coat shells is not found.

The last method we investigated for applying a uniform layer of PVA onto a shell was microencapsulation. Masa Takagi (LLNL) conceived of this concept when working in Osaka, Japan [2–9]. For our purposes, we put a 2% PVA in water solution into a PS shell during the microencapsulation process. This PVA concentration would result in a

~4 µm thick PVA layer on the inside wall of the shell when the solution dried. Water extraction was begun in the same manner used for all 2 mm microencapsulated shells produced at GA. Once a bubble in the PVA solution was nucleated inside the shell, the shell was affixed to and spun on a rotor at ~60 rpm such that the bubble was centered in the shell (see Fig. 2.4–2).

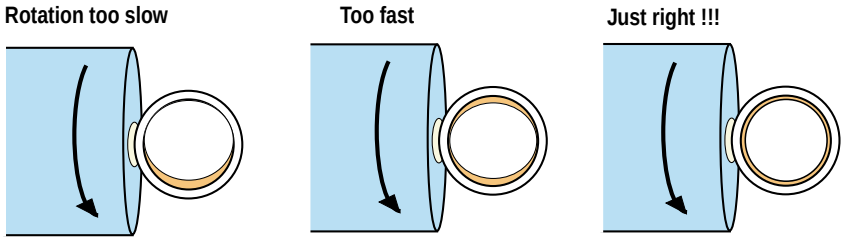

Fig. 2.4–2. A microencapsulated PS shell containing 2% PVA in water solution is spun on a rotor after a bubble has been nucleated. An ~4 µm thick PVA layer is deposited on the inside shell wall when the water is fully extracted. If the shell is spun at just the right speed, the PVA layer will be of uniform thickness.

After two weeks of drying while the shell was spun, interferometry revealed that the resulting PVA layer in the PS shell was very nonuniform. Nevertheless, this first attempt showed much promise. Optimizing parameters such as PVA molecular weight, rotation speed, on-axis alignment, and drying conditions should lead to a much more uniform PVA layer deposition. We intend to pursue this approach next year given appropriate funding.

We took the microencapsulation technique one step further by making a PVA shell. We immersed the PS with PVA shell into toluene. The PS was dissolved away and the PVA shell shown below was retrieved from the bath (see Fig. 2.4–3).

For further information, please contact D. Steinman (GA).

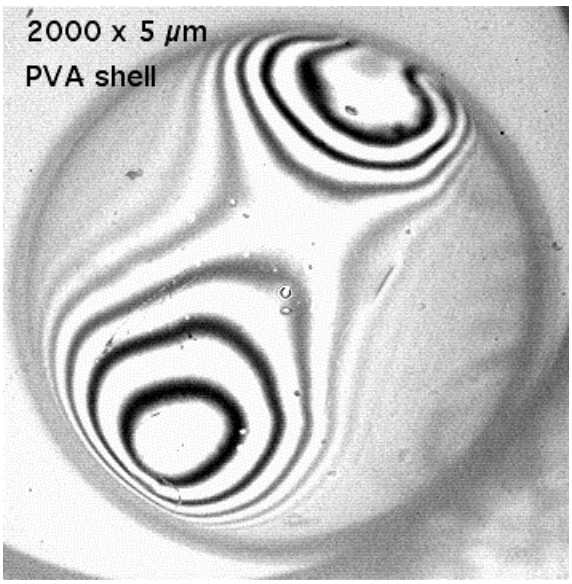

Fig. 2.4–3. A 2 mm PVA shell with a 5 µm wall was made from a microencapsulated PS shell that originally contained a solution of 2% PVA in water. The PS shell was dried while being rotated on its horizontal axis at ~60 rpm. Toluene was used to dissolve away the PS leaving behind the dried inner layer of PVA.

2.5. IMPROVEMENTS IN THE SPHEREMAPPER AND WALLMAPPER

Our AFM spheremapper, now with wallmapper capability, was built over 5 years ago. Several of its components are obsolete — not even maintainable — and some have just proved to have a poor design. In this last year, we have been upgrading the mapper components piece-by-piece. This process is nearly finished; in the process, we are generating a parts list for a new mapper to meet UR/LLE needs.

2.5.1. Computer Controller

The original Mac Quadra used for this is obsolete; we replaced it with a Power Mac G4, replaced the IO boards, and rewrote the LabView controller software to accommodate the new board and function drivers. The new computer is fast enough that we were able to replace the embedded C–code modules with LabView coding, which makes program modification much more simple.

We took the opportunity of the software upgrade to update the user interface and to remove some obsolete code left over from the original development effort. The operator is now presented with a real time view of the data acquisition, rather than being presented with a *fait accompli*. This permits the operator to take corrective measures when data values exceed the range of the instrument. This had not previously been a problem, but as we measure ever larger spheres, we often approach the instrumentation limits. Under these conditions, the revised interface can significantly increase the throughput of the instrument.

2.5.2. Rotating Vacuum Chuck

The original, monolithic vacuum chuck was (1) very hard to manufacture (and therefore hard to replace if damaged) because of the ~150 μm diameter hole required for the tip; and (2) sized for 1/2 mm o.d. shells, which was too big for 0.25 mm o.d. shells and inadequate for >2 mm diameter. We have replaced that design with a two-part chuck; an electroplated, truncated gold cone glued to a hollow aluminum bolt (Fig. 2.5–1). The depth of the truncation is determined by the shell size; each design accommodates a shell diameter range of three times.

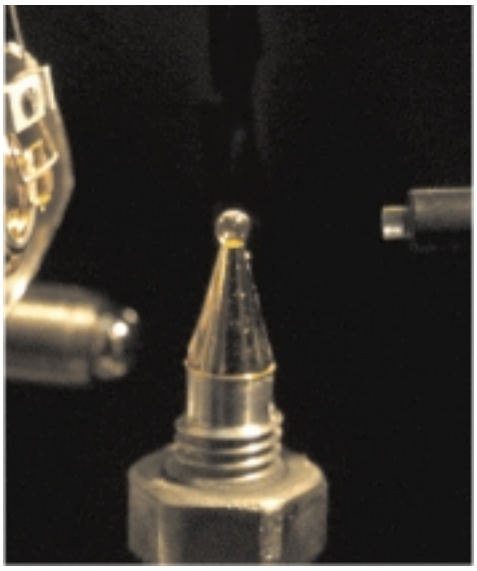

Fig. 2.5–1. 2 mm diameter shell on a new-style rotating vacuum chuck; an electroplated gold cone glued to a hollow aluminum bolt.

2.5.3. AFM

The Digital Instruments stand-alone atomic microscope head used in the current spheremapper is obsolete, cannot be repaired, and is running out of consumable parts. We have bought, but not yet installed, a Dimension 3000 system, which is maintainable and which has an auto touch-down feature that will allow a reproducibly lighter contact force, and a bipolar driver that will allow measurement of shells with larger out of round. Like the computer replacement, this change necessitates replacing many supporting and interfacing components; we expect the final assembly will be more rigid and, therefore, to yield a less noisy measurement than the current system.

For more information contact L. Brown or R.B. Stephens (GA).

2.6. DETERMINING THE PRESSURE AND PERMEATION RATES

Accurate determination of ICF capsule fill-gas pressures has been of critical importance to the ICF laboratories for years. In the past, the fill pressures were confirmed by a variety of time-consuming techniques such as dew point measurement, interferometry, weighing, or by measuring the size of the gas bubble that results when the capsule was broken while immersed in a fluid. A new, relatively inexpensive system designed and constructed by Martin Hoppe and Steve Grant of GA respectively, has the capability to accurately measure the internal pressure inside of 250 μm to 10 mm o.d. ICF capsules in less than 10 minutes per capsule. A picture of this system is depicted in Fig. 2.6–1.

Fig. 2.6–1. Picture of shell pressure/permeation measurement system.

This device is primarily intended for destructive testing. A pointed metal rod is inserted into the sample chamber and held in place just above the glass-to-metal seal by an external magnet (Fig. 2.6–2). After the system has been evacuated and isolated, the

magnet is removed causing the metal rod to fall and crush the shell, thereby releasing its gas load. Measurement of the pressure rise in the system and knowledge of the system volume and shell inner diameter allow for determination of the shell's internal gas pressure.

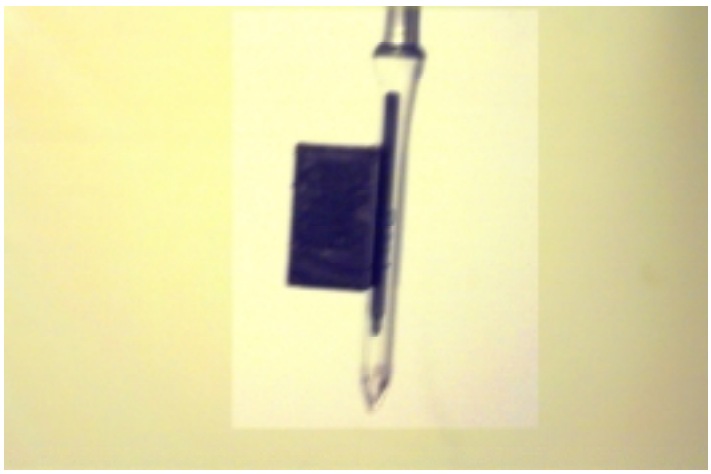

Fig. 2.6–2. Picture of the metal rod suspended in the sample chamber by a magnet. The metal rod is shown lower in the sample chamber than normal for illustration purposes.

The use of either glass-to-metal or metal-to-metal (VCR) seals at all joints results in very low background leak rates (<0.2 mtorr/h) and very fast pump down times. In addition, a high quality Baratron pressure gauge (0.1 to 10,000 mtorr range with an accuracy of 0.05% plus an offset correction) allows for very accurate pressure measurement. The data shown in the Table 2–1 illustrates the capabilities of this system.

TABLE 2–1
MEASURED SHELL PRESSURE IN PAMS SHELLS STORED IN AMBIENT CONDITIONS

Shell No.	Shell Inner Diameter (μm)	Measured System Pressure (mtorr)	Calculated Shell Pressure (atm)	Shell Fill Pressure (atm)*
1	2594	602±1	0.98±0.01	0.987±0.005
2	2343	447±1	0.98±0.01	0.987±0.005
3	2353	454±1	0.99±0.01	0.987±0.005
4	2578	592±1	0.98±0.01	0.987±0.005
5	2383	473±1	0.99±0.01	0.987±0.005
6	891	76.5±0.5	3.07±0.07	3.10±0.05

*Pressure as measured by an independent gauge during the permeation filling procedure. Although this device is primarily intended to be destructive in nature, a precision sample heating block has been added which allows for nondestructive evaluation of capsule gas-fill half-lives at temperatures up to 160°C.

For additional information contact Dr. M. Hoppe or D. Steinman (GA).

2.7. POLARIZED LIGHT FOR DETECTING DEFECTS IN PAMS SHELLS

A continuing problem in shell wall characterization is the accurate surveying of the entire two-dimensional surface. Our spheremapper and wallmapper yield information only along isolated one-dimensional paths. Commercial interference microscopes (Wyko RSI, for instance) give two-dimensional information, but only on small patches. Therefore, we were surprised and intrigued when we noticed that a complicated fringe pattern appeared when viewing a shell under crossed polarizers. Matt Worstell, a student, investigated the phenomena this summer, and after a discussion with Mark Wittman (UR/LLE) we now understand the phenomenon: it shows the difference in thickness between the front and back wall of the shell with a fringe for every ~0.1 μm of thickness difference. These fringes are visible over most of the shell image; by rotation, we can quickly examine the entire surface for thickness anomalies. We expect this phenomena to be critical to the future selection of deliverable shells. The following sections describe the phenomenon we discovered.

2.7.1. Shell Optics

The image of a shell is predominantly formed by rays which are transmitted through every surface; the most important reflected waves are less intense by about two orders of magnitude (Fig. 2.7–1). But these reflected rays contain important information about the local wall thickness: (1) their path length is longer by about twice the thickness of the shell; and (2) there are a pair of distinct rays at every point in the image — one with the extra reflection in the front surface, and one with that in the back. So long as the path difference between these two rays is less than the coherence length of the light, they will interfere, and the image they form will show fringes for every $\lambda/4n$ (~0.1 μm) difference.

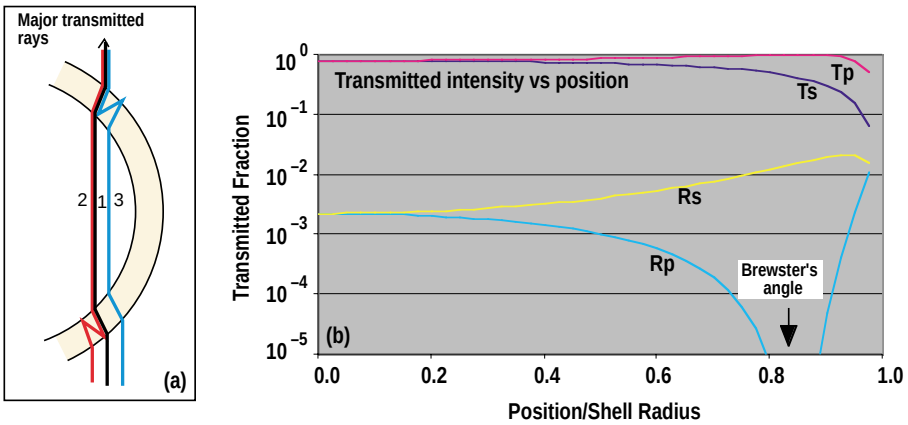

Fig. 2.7–1. (a) Most intense transmitted rays through a shell; #1 is transmitted through all surfaces, while the other two have a pair of reflections, #2 in the back surface and #3 in the front surface. (b) Intensity of the transmitted beams (T = transmitted only, R = two reflections) as a function of polarization (s = radial, p = tangential).

2.7.2. Observation Optics

The key to observing these fringes is in noting that the two extra bounces polarize the reflected rays much more than the waves which are simply transmitted (Fig. 2.7–2). As a result, putting the shell between crossed polarizers will change the relative strength of the straight-through and the twice-bounced waves to the point that one can see the oscillations in intensity of the latter. Since the polarization effect at every point is along

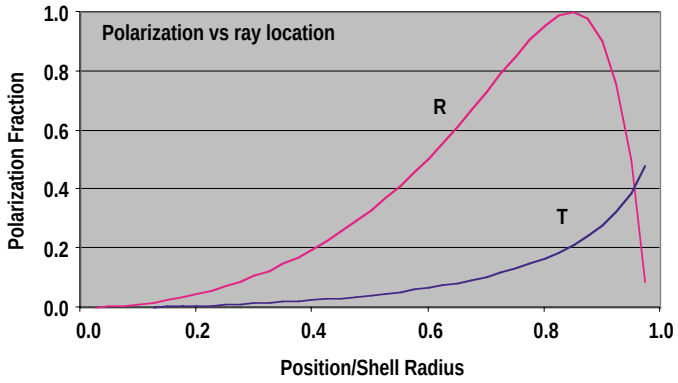

Fig. 2.7–2. Polarization of transmitted beam induced by transmission through and reflection from shell surfaces for T = ray transmitted through all surfaces and R = ray with two extra reflections in shell wall.

the tangential direction image, one does not use linear polarizers to see these fringes; they are ineffective for radii along one of the polarizer axes [Fig. 2.7–3(a)]. Instead, we use a polarizer and quarter-wave plate to produce circularly polarized light, another quarter-wave plate to produce linear polarization (from unmodified rays), and a final, crossed polarizer to block all unmodified light from reaching the detector. The shell is illuminated

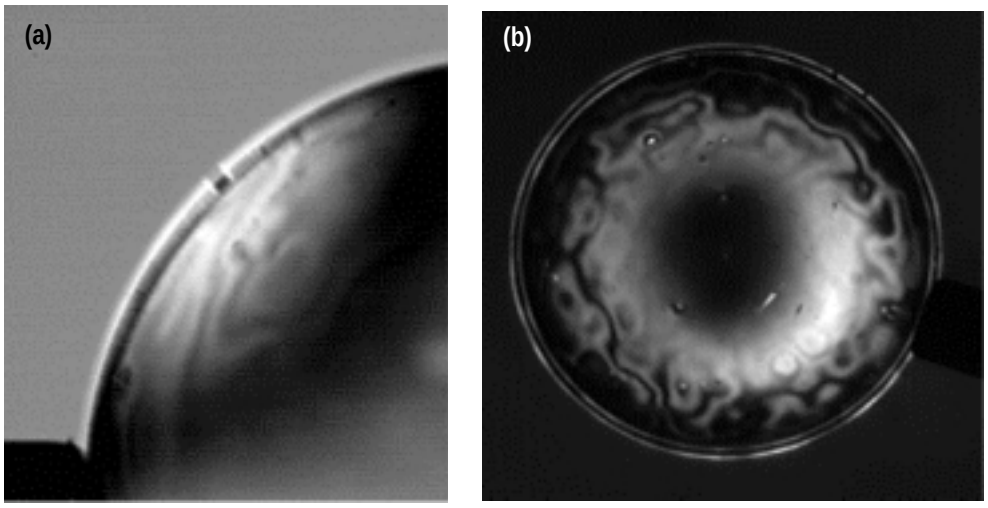

Fig. 2.7–3. Similar shells imaged with (a) linearly polarized light and (b) with circularly polarized light.

with light which has been collimated, to limit blurring of the fringes, and filtered, to limit the spectral width and increase the coherence length to ~2.5 μm. These additions give bright fringes visible all around the shell [Fig. 2.7–3(b)]. Fringes disappear toward the center as the rays approach normal incidence and the transmitted intensity goes to zero. Note that this is just a lack of light; the fringe contrast remains about constant.

2.7.3. Image Feature Interpretation

There are several sources of fringes in these images. Figure 2.7–3(b) shows two of them: (1) local rings from isolated defects like the vacuole at about 11 o'clock can be seen to move with the shell, and (2) overall wall thickness variations which flow and reform on rotation as different front and rear features are superimposed on each other. Figure 2.7–4(a) shows a third type of fringe which appears even on perfectly uniform shells. You can see from Fig. 2.7–1(a) that the radial position of the back wall ray path

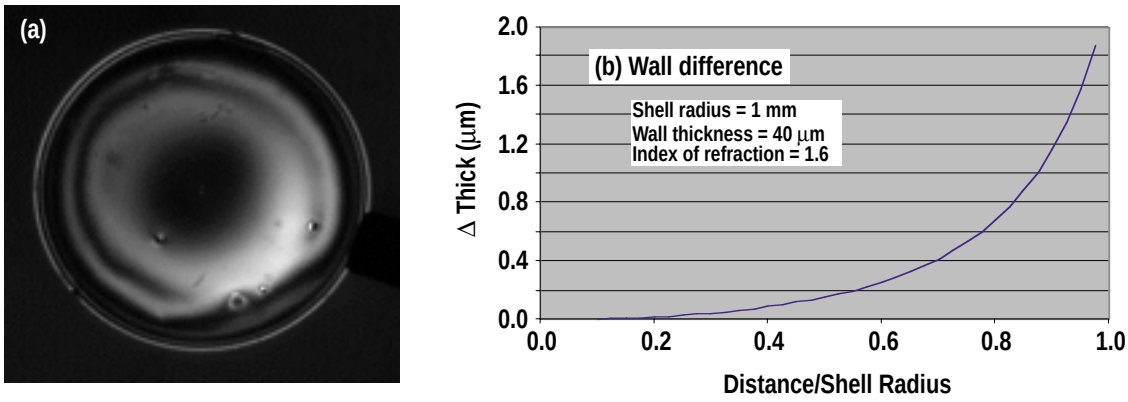

Fig. 2.7–4. (a) PAMS shell with uniform, but rather thick walls (32 μm); and (b) the front-to-back difference in wall thickness sampled by a ray coming out of the front from a single point.

(ray #2) is slightly inside that of the front wall ray path (path #3). As a result, the effective wall thickness

$$d_{eff}(r) = d/\cos\left(\sin^{-1}\left\{\sin\left[\sin^{-1}(r/R)\right]/n\right\}\right) ,$$

$$= d/\cos\left[\sin^{-1}\left(\frac{r}{nR}\right)\right] ,$$

$$= d\Big/\left[\sqrt{1-\left(\frac{r}{nR}\right)^2}\right] ,$$

where d is wall thickness, n is the index of refraction of the shell, r is the distance from the shell center, and R is the shell radius is different for the two rays [Fig. 2.7–4(b)]. For a thick shell wall, this difference is sufficient to show rings just inside the edge of the shell image. These rings are sensitive to the total wall thickness, will appear only for fairly thick walls, and will move in and out only if the wall in that region changes substantially.

For more information contact R.B. Stephens (GA).

2.8. REFERENCES FOR SECTION 2

[2–1] M.J. Block, "Surface Tension as the Cause of Benard Cells and Surface Deformation in a Liquid Film," Nature **178**, 650 (1956); C.V. Sternling and L.E. Scriven, "Interfacial Turbulence: Hydrodynamic Instability and the Marangoni Effect," AICHE Journal **5**(4), 514 (1959); J.C. Berg, A. Acrivos and M. Boudart, "Evaporative convection," Advances in Chemical Engineering **6**, 61 (1966); M.F. Schatz et al., "Onset of Surface-Tension-Driven Benard Convection," Phys. Rev. Lett. **75**(10), 1938 (1995).

[2–2] O. Pirotte and G. Lebon, "Surface-Tension Driven Instability in Spherical Shells," Appl. Microgravity Technology **I**(4), 175 (1988); H.C.J. Hoefsloot and H.W. Hoogstraten, "Marangoni Instability in Spherical Shells," Appl. Microgravity Technology **II**(2), 106 (1989); O. Pirotte and G. Lebon, "Comments on the Paper 'Marangoni Instability in Spherical Shells'," Appl. Microgravity Technology **II**(2), 108 (1989).

[2–3] M.L. Hoppe, "Large Glass Shells from GDP Shells," Proc. 13th Target Fabrication Specialist Meeting, Catalina Island, 2000, to be published in Fusion Technology; General Atomics Report GA–A23356 (2000).

[2–4] M.L. Hoppe, "Fabrication of Glass and Titania Shells by Pyrolysis of Doped GDP," General Atomics Report GA–A22995 (1998) p. 2–7.

[2–5] Project Staff, "Inertial Confinement Fusion Target Component Fabrication and Technology Development Support, Annual Report to the U.S. Department of Energy, October 1, 1998 through September 30, 1999," J. Gibson, ed., General Atomics Report GA–A23240 (1999).

[2–6] S. Timoshenko, Theory of Elastic Instability, (McGraw-Hill, New York, 1936).

[2–7] Laboratory for Laser Energetics Review 81, pp. 6–11.

[2–8] F.Y. Tsai et al., Fusion Tech. **38**(1), 83 (2000).

[2–9] Private communication between D.A. Steinman and Masa Takagi, July 2000.

3. FOAM TARGET DEVELOPMENT

Interest in polymeric foam materials for Inertial Confinement Fusion (ICF) target components has increased markedly in the past year. We were requested to develop, fabricate, and deliver a variety of foam components for ICF targets in FY00.

For the purposes of this report, "low-density foams" are defined as polymeric foams with densities of 50 mg/cm^3 or less. Requests for low-density foams came from two facilities — Sandia National Laboratory (SNL) and Naval Research Laboratory (NRL). While each facility requested some production, the emphasis was strongly on development — development of new casting techniques, development of embedding techniques, developing of coating techniques, and development of new foam systems. The overlap between the requests led to a synergism that was beneficial to both tasks. Most notably, the NRL request for a CH foam with approximately 1 μm cell size lead to research of a divinyl benzene (DVB) foam system that can be made with deuterated monomer to meet SNL's diagnostic needs.

3.1. LOW-DENSITY FOAMS PRODUCTION FOR SNL

FY00 is the fourth year that SNL has requested a subtask designated solely to produce low-density foams. There were two laboratories set up to do this work, one at the Schafer Livermore facility and one at SNL. The Schafer Laboratory was headed by Kelly Youngblood and was responsible for three main categories of components: components that required coating, components that required extensive mold development, and batches of foam components all of the same dimensions. The SNL laboratory was headed by Diana Schroen-Carey and was responsible for components too fragile to ship and components that required process development.

The foams requested this year were of much more complex geometries than in prior years, these geometries being the result of combining smaller individual foams into larger, more complex foam components. For example, the most requested geometry was a cylinder with two radiation entry hole (REH) foam tabs, see Fig. 3.1–1. The foam replaces a target foam and two hole-closure foams. The single foam design has the advantage that there are no gaps between the target foam and the hole-closure foams, thus the wire plasma cannot prematurely enter the REH.

Another example of multiple components redesigned into one is a component with an embedded diagnostic for spectral studies. The first component of this type had a thin metallic foil (Mg/Al) embedded 2 mm from one end, see Fig. 3.1–2. The greatest

difficulty in fabrication of this component was due to the fact that the foil was only 400 μm smaller in diameter than the diameter of the foam. This left only a 200 μm ring of foam for connection of the two foam sections.

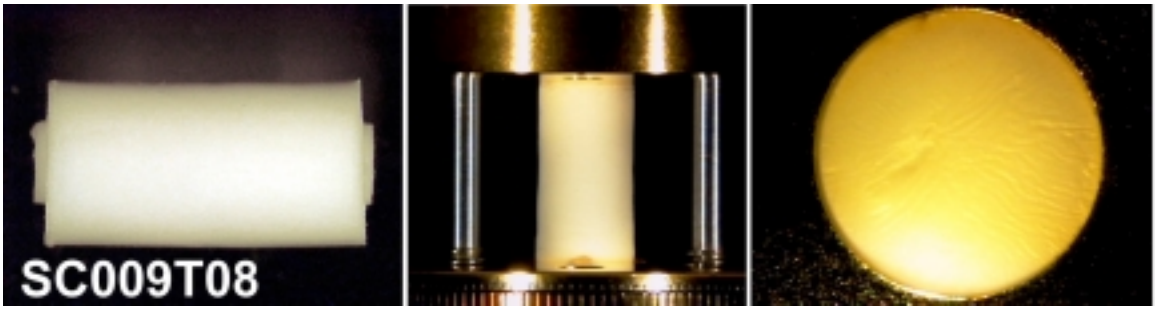

Fig. 3.1–1. Double-REH tab foam. The far left photo shows the foam as made. It is 14 mg/cm^3 TPX, 9.6-mm long main cylinder, 5.0-mm main diameter with two 2.4-mm diameter tabs, each 0.4-mm tall. These tabs fit into the wafer and the castle as shown in the center photo. The far right photo shows an end on view of the REH with the close tolerance fit of the foam tab.

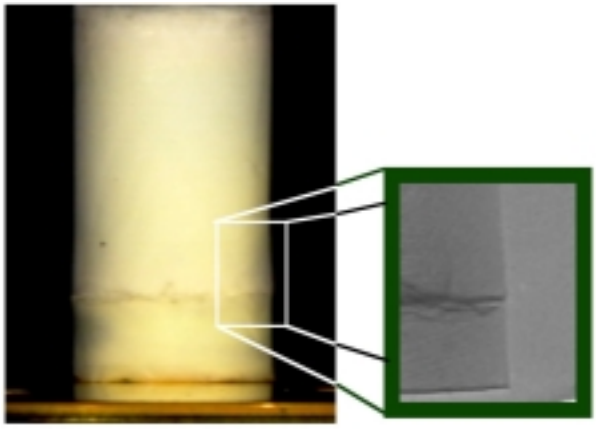

Fig. 3.1–2. The foam pictured here contains a foil embedded 2 mm from the bottom hardware. The foam was cast sequentially so that the two sections melded together and required no glue for fabrication. The foil was 0.2 μm of parylene, 0.2 μm of Mg (in multiple layers) and 0.2 μm Al (also in multiple layers). The image to the right is a radiograph showing the foil within the foam. The foam is 9.6-mm tall, 5-mm diameter and has a density of 14 mg/cm^3. We wish to thank Larry Ruggles of SNL for the numerous radiographs he did throughout the development and fielding of all the target foams.

Another component with an embedded spectral diagnostic was a foam cylinder 20-mm tall, 10-mm in diameter, density of 5 mg/cm^3 with a polystyrene (PS) rod embedded down its center. The PS rod was coated with MgF. A radiograph of this type of foam is shown in Fig. 3.1–3.

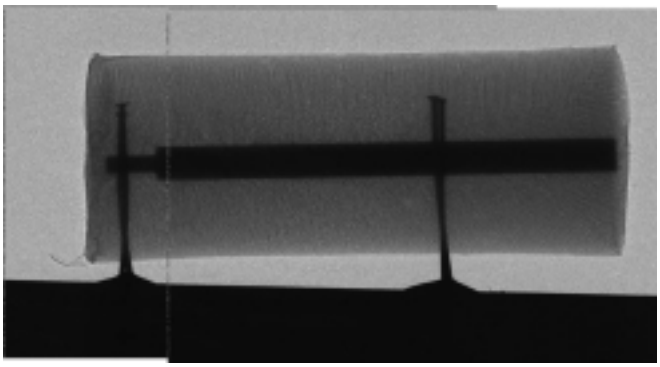

Fig. 3.1–3. This radiograph shows an embedded PS rod in a 5-mg/cm^3 TPX foam cylinder.

The most difficult component to fabricate within tolerances was a 5-mg/cm^3 foam with an embedded sphere. This component was originally designed as an annulus with two plugs. The inner diameter of the annulus was just slightly greater that the diameter (2 mm) of the capsule. To hold the capsule at the midpoint in the z-direction, there were to be two equally tall foam plugs. This design would have presented an extreme assembly challenge, as all of the foam components were to be of 5-mg/cm^3 density. The final design was a single foam cylinder with an embedded capsule. The mold had an alignment fixture that allowed for placement of the capsule to within specified limits. The resultant foam is shown in Fig. 3.1–4.

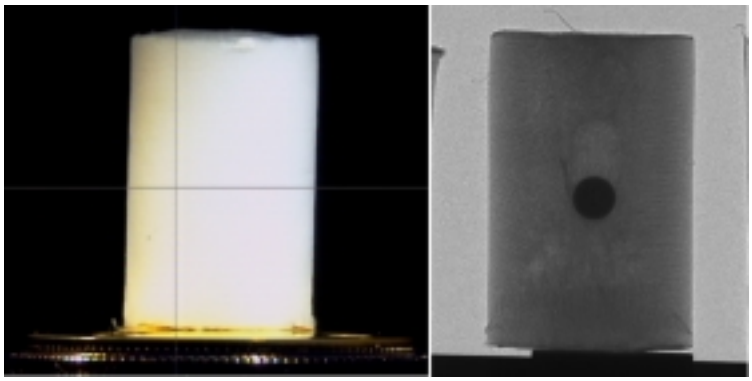

Fig. 3.1–4. The photo on the left shows the foam target used in the second shot of the series. The cylinder is 10-mm diameter, 15-mm tall, 5 mg/cm^3. In the center of the foam, a 2-mm gas filled capsule has been embedded; the radiograph on the clearly shows the capsule.

We believe that this target represents many firsts:

- The first time a capsule has been embedded in a freestanding foam.
- The first time a capsule has been embedded in foam fabricated from a polymer composed of only carbon and hydrogen.

- The first time a capsule has been embedded in a foam having a density of less than 10 mg/cm^3.
- The first time a capsule had been embedded in a coated foam.
- The first time a gas filled capsule has been embedded in a foam.

The fact the capsule was gas filled added a great deal of complexity. All of the processing had to be done within a very short time span to provide the desired gas-fill at shot time. This required coordination with General Atomics (GA) to deliver the capsules at the appropriate time, three capsules to Schafer Laboratory in Livermore (for the three gold-coated targets) and three capsules to SNL (for the three bare foam targets). The tight time requirements dictated that both foam labs cast at the same time and that Steve Dropinski from the SNL lab fly to Livermore to mount the foams on machine hardware (prior to coating) and then fly the finished components back, see Fig. 3.1–5.

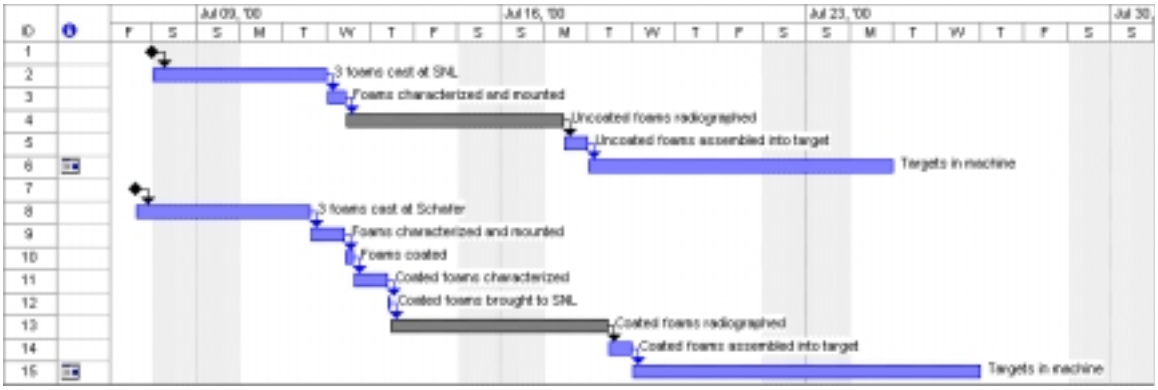

Fig. 3.1–5. This is the timeline that was used for producing the targets at both facilities. The black diamonds indicate when the capsules had to be delivered for casting.

The timeline was planned using the measured half-life, 40 days, and the initial D_2 pressure, 15 atm that would give a 12 atm fill at shot time. However, there is now some confusion as to what the pressure was. A total of four witness shells were burst to determine gas pressure. Two shells were held at GA until shot time. They each had 12 atm. Two additional shells were delivered to the foam labs, cast in foams, one foam was gold-coated, both foams were characterized and radiographed. At shot time, they were sent back to GA and the tested pressure was 6 atm. GA is currently testing new shells by exposing them to the conditions that the foam cast shells were exposed to (high temperatures, high humidity and solvent from the foam casting) to determine which factor(s) degraded the gas holding capability of the shells.

Of the six components with embedded capsules, three were gold coated. There are two issues associated with coating open cell foams. The first is the difficulty in characterizing and modeling the coating after it has been applied to the open structure of

the foam. Coating deposition is a line-of-sight process, so the coating is deposited in a discontinuous manner at various depths of the foam, as is depicted in Fig. 3.1–6. To overcome this effect, we were developing a process to place a sub-micron formvar coating at the outer boundary of the foam structure. This process was not fully developed for this series, but we hope to field it the next time a coated foam component is requested.

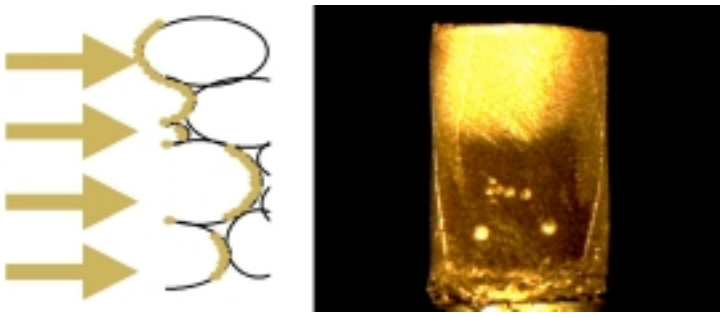

Fig. 3.1–6. The left side image is a schematic of a coating on an open cell foam. The right side image is a prototype foam whose upper half had the Formvar undercoating. The gold coating over the Formvar has the classic gold color and appears to be continuous. The lower half of the foam shows the diffuse brown coating caused by the gold deposition throughout the foam structure.

The second issue with coating a foam is the temperature sensitivity of the foam. The glass transition temperature of the TPX foam is approximately 80°C. Thus, the foam surface could not exceed that temperature at any time during the coating process or the foam would be deformed. Using very careful processing, Ed Hsieh and Brian Motta were able to coat between 100 and 3500Å without deforming the foam. We expect to extend that coating range and to develop similar ability to coat with Al in the upcoming year.

We have discussed many foam geometries in this report. It is important to recognize that for each geometry there had to be a mold. The molds are precision pieces of work, often requiring significant engineering in their design. Each mold must be compatible with the foam system. For resorcinol-formaldehyde or PS, the reactivity of the foam system must be considered. For TPX, the thermal conductivity is critical. The machinists responsible for this effort are Pat Collins and Scott Faulk. Examples of their work is shown in Fig. 3.1–7.

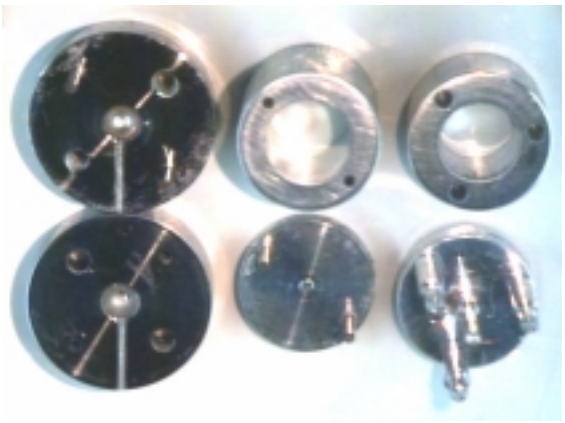

Fig. 3.1–7. These parts are the pieces of three molds. The far left pieces, top and bottom, produce a spherical foam. The middle pieces produce a cylinder 20-mm tall, 10-mm in diameter, with a center alignment feature for embedding a PS rod. The far right pieces produce a cylinder, with a center pin for exact placement of a capsule within the cylinder. The pin is removed before the foam is completely gelled to allow the solution to backfill the pin location and produce a uniform foam.

3.2. FOAM DEVELOPMENT

The foam development task focused on research into a lower cell size foam, produced from a pure CH polymer. This work started as an NRL project but quickly gained the attention of SNL. The foam we are investigating is polymerized from DVB, and is built upon the work of Warren Steckle [Los Alamos National Laboratory (LANL)] [3–1] and Steve Letts [Lawrence Livermore National Laboratory (LLNL)] [3–2]. When polymerized in a simple solvent system, the cell size can be approximately 1.5 μm for 10 mg/cm^3 foam as can be seem in Fig. 3.2–1.

A 1.5 μm cell size is too large for optical transparency, but an optically transparent foam would have correspondingly thinner cell walls. The 1.5 μm cell size equals thicker cell walls and improved mechanical strength. This is advantageous not only for handling the foam, but also for the strength required for filling with cryogenic hydrogen and its isotopes. It should be emphasized that while this foam is mechanically stronger than a carbon aerogel, it is by no means robust. Removal of the foam from the mold remains the most difficult step in fabricating components. While we sincerely hope that future work will yield a higher percent of successful parts, we have begun producing trial pieces. At densities of 10 and 20 mg/cm^3, we have produced ovals 2 by 5 mm, 200 μm thick. At a density of 14 mg/cm^3, we have produced prototypes of the double-ended REH foam as shown in Fig. 3.2–2. This foam is scheduled to be shot on the Z machine by LANL experimenters using fully deuterated DVB. (LANL is supplying the deuterated DVB

monomer.) The fully deuterated DVB foam enables the use of neutron diagnostics — something that has been of great interest to both SNL and LANL.

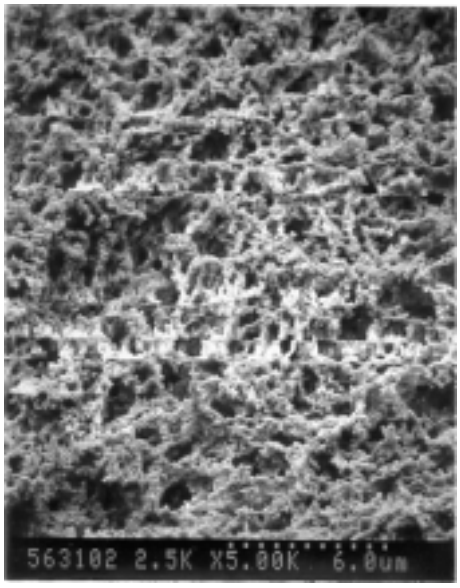

Fig. 3.2–1. This scanning electron microscope (SEM) shows the cell size and morphology of a 10 mg/cm^3 DVB foam.

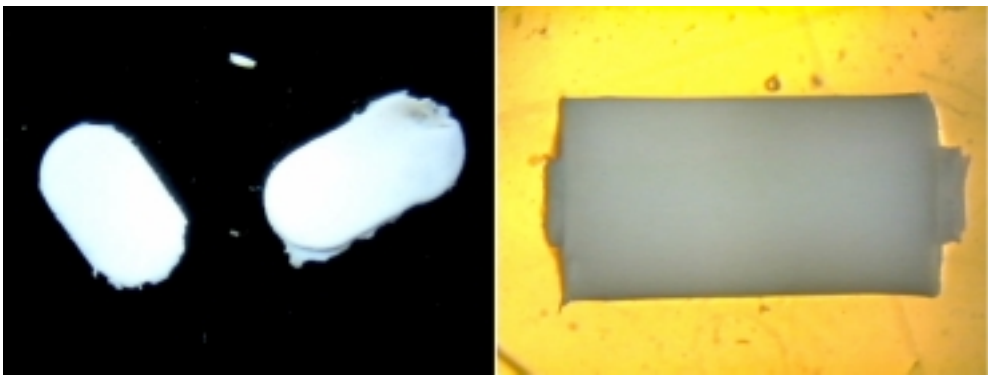

Fig. 3.2–2. These two pictures are samples of DVB foams that have been produced.

The DVB system may also be of interest for another reason. It can be used in an emulsion procedure analogous to the PS foam procedure developed by LANL and LLNL [3–3]. An SEM of this type of foam is shown in Fig. 3.2–3. The emulsion polymerization and the simple solvent polymerization of DVB opens up some interesting possibilities. By using the two procedures, the same polymer at the same density can be produced with cells sizes of ~1.5 or ~15 µm. This may be useful for studying the effect of foam cell size in experiments.

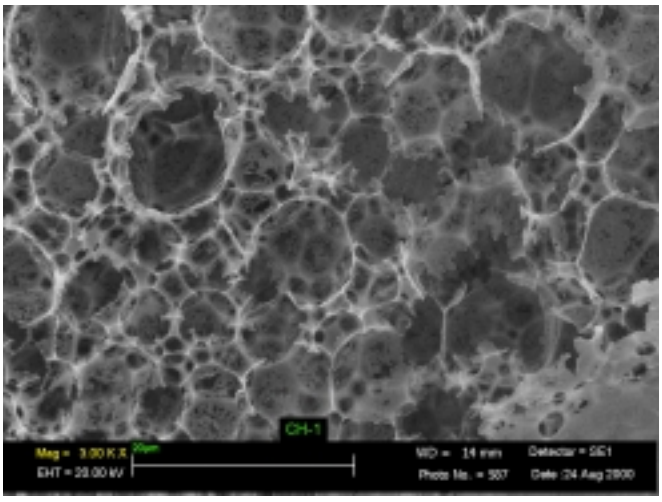

Fig. 3.2–3. This SEM shows the larger cell size that can be obtained by using an emulsion procedure to obtain a 10 mg/cm^3 DVB foam. We expect the work with DSVB to be a large effort in the upcoming year.

For further information, please contact D. Schroen-Carey (Schafer).

3.3. MICROMACHINED FOAM SHELLS

Initial experiments were performed at GA this fiscal year to investigate the feasibility of producing spherical shells by micromachining. The desired component is a glow discharge polymer (GDP)-coated foam PS shell, diameter in the vicinity of 5 mm, with a PS thickness in the vicinity of 150 µm, and a GDP thickness sufficient to prevent rupture with a pressure differential of about 1.7 atm.

Two conceptually different techniques were explored. The first one was a right-side-out (RSO) method, in which foam hemispherical shells are machined and are subsequently joined at the equator, following which the shell is coated with GDP. In the second technique, an inside-out (ISO) method, a thin GDP coating is applied to a micromachined copper mandrel, which is subsequently leached away, creating a GDP mold for a foam hemisphere. In this latter technique, after the foam filling the GDP mold is machined to create a 150 µm thick wall adjacent to the GDP, the hemishells are joined and recoated with GDP.

In the RSO method, PS foam with a density of about 250 mg/cm^2, obtained from Schafer Corp., was used to micromachine hemishells with a wall thickness of about 160 µm. They were made in matching pairs, with a tapered joint at the equator. The general techniques employed are quite similar to those mentioned in the last annual report for machining foam hemispheres [3–4].

The male-female pairs were assembled with a vacuum assist that arises due to the connected porosity of the foam. After the taper-jointed halves are properly positioned, they are held together by a pressure differential ΔP of

$$\Delta P = \left(P_a - P_c\right)\left(\frac{1 - \sin\theta}{2}\right)$$

where θ is the north latitude below which the exterior of the shell is exposed to ambient pressure and above which there exists a vacuum, P_a is the ambient pressure, and P_c is the pressure in the evacuated conical holder («P_a). This relation follows directly from the assumption that the porosity of the foam is uniform, which is quite likely, and that the flow is Knudsen, which is probably not the case, except in the vicinity of the North Pole.

In our configuration, wherein pumping occurs above the approximate latitude of Portland, Oregon (45°), the calculated pressure differential is about 15 kPa. The estimate of the internal pressure assumes that the conductance of the polystyrene foam is isotropic, and that it is independent of pressure in the regime considered here (Knudsen flow). The validity of this assumption is perhaps not well founded for the following reason: SEM analysis of this foam showed that the holes connecting the pores were of the order of 1 μm in diameter; the pores themselves were in the range 5 to 20 μm in diameter. The mean-free path of gas atoms is about 1 μm at a pressure of ~0.4 atm. Thus, at pressures well below ~0.4 atm, Knudsen flow between the pores would occur, and the conductance would be pressure independent. At 0.4 atm and higher, transition flow through the connecting holes will predominate and the conductance would no longer be entirely independent of pressure. The flow in the pores would be in the transition regime throughout and, therefore, pressure dependent — probably decreasing the pressure inside the shell compared to the simple model. Ignoring the probable complexities of the situation, the estimated pressure drop across most of the shell would be about 0.15 atm (15 kPa), but over the conical cavity it would be nearly 0.7 atm. The 15 kPa holding pressure keeps the hemishells in place while cement is applied. A foam hemishell and a spherical shell produced by connecting two hemishells are shown in Fig. 3.3–1

Only one such shell has been coated with GDP and it has not yet been tested for gas-fill hold-time or bursting pressure, nor has it been characterized for surface finish or out of round.

To investigate the feasibility of the ISO method, five hemispherical copper mandrels were micromachined and coated with GDP to a thickness between 6 and 10 μm. They were shipped to SNL where the copper will be leached away and the remaining GDP will serve as a mold for producing a foam hemisphere. The SNL portion of the task was not completed this fiscal year.

Fig. 3.3–1. A 5-mm diam PS foam hemishell rests upon FDR's cheekbone, while two such hemishells, glued together, rest behind his ear. The foam density is about 250 mg/cm^3 and the wall thickness is 160 μm. The GDP coating has not yet been applied to this shell.

3.4. REFERENCES FOR SECTION 3

[3–1] Warren P. Steckle, Jr., et al., "Carbon Foams Prepared from Hyper-Cross-Linked Polymer Foams," Polymeric Foams Science and Technology ACS Symposium Series 669 (1997).

[3–2] Private communication between Diana Schroen-Carey and Steve Letts.

[3–3] B.L. Haendler et al., "Low-Density Hydrocarbon Foams for Laser Fusion Targets, Progress Report — 1987," Lawrence Livermore National Laboratory Progress Report UCID-21080-87 (University of California, 1987).

[3–4] Project Staff, "Inertial Confinement Fusion Target Component Fabrication and Technology Development Support, Annual Report to the U.S. Department of Energy, October 1, 1998 through September 30, 1999," J. Gibson, ed., General Atomics Report GA–A23240 (1999).

4. PLANAR TARGET DEVELOPMENT

During this year, the task descriptions and requests for targets for the NIKE and OMEGA laser programs have been similar to those of previous years with increasing emphasis on foam targets for the Naval Research Laboratory (NRL). Throughout the year, both NRL and the University of Rochester/Laboratory for Laser Energetics (UR/LLE) have refined their target requirements and have requested new types of targets that require rapid development of production techniques.

4.1. NIKE LASER TARGETS

NIKE target requirements have continued to shift toward cryogenic targets. During FY00, the majority of the targets we shipped to NRL have been mounted on cryogenic target mounts (CTMs) rather than polymer NIKE target frames. The targets have also become more and more complex. More of the targets have patterns imposed on one surface, multiple layers of polymer and metal, and complex geometries.

4.1.1. Planar Targets

We continue to deliver some classic flat-film polymer targets mounted on polycarbonate frames (Fig. 4.1–1) to NRL. Nearly all flat-film polymer targets are made with polystyrene (PS) that we cast to precise specifications. Target thickness are usually required to be within 1 μm of a nominal thickness that can range from 10 μm to well over 100 μm. The thickness of each target must be uniform over the entire area of interest and must be reported with a precision of one-tenth of a micron. The surface must be smooth with no accidental perturbations greater than 25Å measured peak to valley. The films must also be very flat when mounted with maximum allowable curvature of 1 μm of curvature over 1 mm laterally. We are able to consistently produce flat, smooth films by casting PS on a flat substrate, usually a silicon wafer. After the PS dries into a stiff film, it is annealed at 100°C for about two days to remove stresses in the film.

Flat film targets have been delivered with sinusoidal and step-ramp patterns impressed on one side of the film. These are made by casting the PS on a patterned mold, usually made of silica. Molds with a range of patterns are available and will be discussed in a later section.

We have used one or the other of two primary methods for adding metallic coatings to polymer films if the specifications dictate. For thicker coatings (above ~100Å) of

aluminum or gold, we used evaporative coating. Our evaporative coater is being outfitted with a thickness monitor, but we have been able to control coating thickness by controlling the amount of material placed on the heater, the current through the heater, and the time of deposition. Coated layer thickness are characterized by using an interferometer or a profilometer to measure the thickness of film deposited on a witness plate. The other method we use for coating films with metal, particularly for thin layers, is a sputter coater. With the sputter coater, the thickness of the film can be monitored as the film is deposited. After deposition, we confirm the thickness of the deposited layer using the same techniques as we use for characterizing evaporated films.

Fig. 4.1–1. NIKE target frame with polymer film target.

Most of the targets NRL requires are designed to work in a cryogenic environment. The targets have various configurations, but usually have certain things in common. All the cryogenic targets we made for NRL during FY00 consisted of an aluminum cryogenic target mount (Fig. 4.1–2) and most had a covering of polyimide film.

The simple polyimide films for the NRL targets have been obtained commercially or spin cast in our Schafer Corporation laboratory. The films we make at Schafer are normally 1.5 μm thick, but have been as thin as 50 nm. Thicker films, usually 13 μm, are available commercially. These commercially available films often are not smooth and have imbedded impurities and flaws, but if the requirement is only for a cryogenic pressure seal, they are adequate and less expensive than the high-quality films we make.

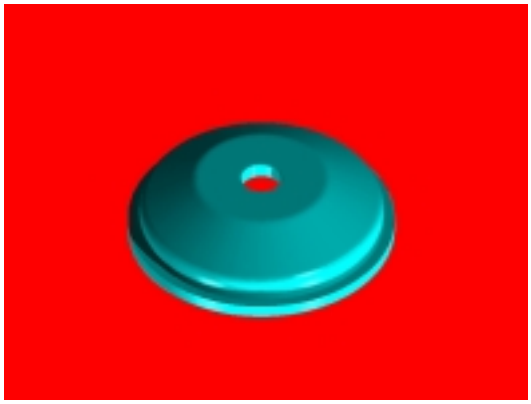

Fig. 4.1–2. Aluminum cryogenic target mount.

During FY00 NRL requested an increased number of polyimide films with a sine wave pattern impressed on them. We spin cast 1.2 to 1.5 µm of polyimide on a patterned mold. This results in a thin polyimide film that is corrugated. Casting on a pattern with 0.5 µm peak-to-valley modulation generally results in about 0.2 µm of modulation in the mounted polyimide. This technique maintains a high degree of mass uniformity in the polyimide while imposing a sine wave pattern onto material (such as liquid deuterium) that is in contact with the polyimide (Fig. 4.1–3).

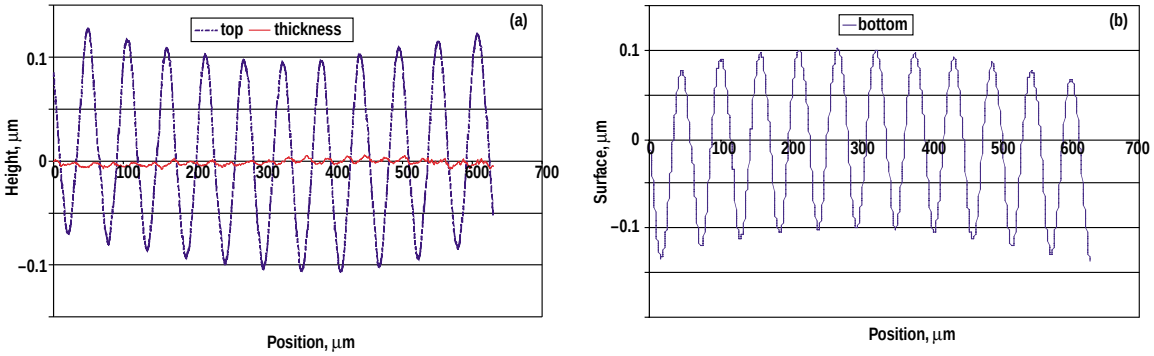

Fig. 4.1–3. Wavy polyimide characterization. Top surface and bottom surface match closely giving very little mass variation.

4.1.2. EOS Targets

This year, we began development of a new type of equation of state (EOS) targets for NRL. These EOS targets consist of a machined 60 µm aluminum plate and a 50-µm thick resourcinol-formaldehyde foam accurately separated by 50 µm using spacers. The assemblies are mounted on a polymer film attached to a CTM.

The specification for this series of EOS targets is depicted in Fig. 4.1–4. To implement the design, we machine a 60-µm thick aluminum plate with 100 µm high supports on each end. Walls are actually curved slightly because the plates must be machined on a lathe and cut out from a circular piece. The base plates are attached to a 13-µm thick layer of commercially procured Kapton which has been stretched over a CTM. The 50-µm thick layer of resorcinol-formaldehyde (RF) foam must be mounted 50 µm above the aluminum base plate. Additionally, the top and bottom surfaces of the foam must be marked with an aluminum stripe. The aluminum serves two purposes: it provides a well-defined optical surface for characterization, and it gives a diagnostic x-ray flash during the experiment when the shock wave reaches each foam surface. For characterization, the bottom stripe must be wider than the top stripe so it is visible after the target is assembled. We make each stripe 100 nm thick. The top strip is 100 µm wide and the bottom stripe is 200 µm wide. The foam must be mounted to a support that can be attached to the spacers on the base plate. We use a piece of glass coverslip that is about 180 µm thick. A hole drilled in the center of the coverslip allows characterization without sacrificing rigidity. For some designs, we stretch a 6 µm sheet of polyimide over the hole to support the foam; other designs use a PS support surrounding the foam laterally.

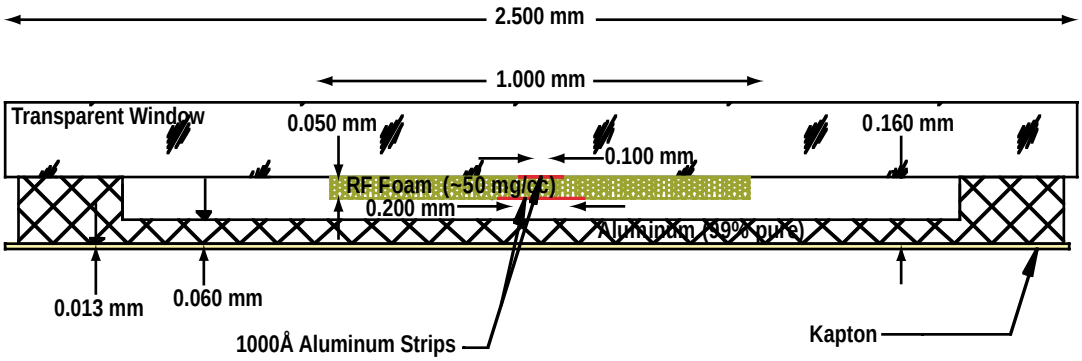

Fig. 4.1–4. Drawing of EOS target with 50 µm RF foam mounted above 60 µm Al base plate. Aluminum stripes define the two foam surfaces.

The design of these targets is nearly complete. We expect to deliver targets for a campaign early in FY01.

A list the pattern substrates currently available at Schafer for casting is listed in Table 4–1. Some of the substrates listed in the table are starting to degrade from continued use. In some cases, pits are forming in the surfaces and in others particles cannot be removed or some other surface flaw interferes with the usability of the mold. We have ordered replacements for gentec#1B (two molds with the same pattern are not much more expensive than one) and will probably have to replace others as well.

TABLE 4–1
PATTERN SUBSTRATES

Substrate Number	Surface Function	P-V Amplitude (μm)	Wavelength (μm)
Gnd Quartz #3	Random rough	3 um grit	
Gentec #01B	Sin(x)	0.23	12.0
Gentec #03	Sin(x)	0.10	60.0
Gentec #04	Sin(x)	0.25	60.0
Gentec #06	Sin(x)	0.25	20.0
Gentec #07	Sin(x)	0.10	30.0
Gentec #08	Sin(x)	0.25	30.0
Gentec #09	Sin(x)	0.50	30.0
Gentec #10	Sin(x)	0.50	20.0
Gentec #11	Sin(x)	1.00	20.0
Gentec #12	Sin(x)Sin(y)	0.10	30.0
Gentec #13	Sin(x)Sin(y)	0.10	60.0
Gentec #14	Sin(x)	0.47	60.0
Gentec #15	Sin(x)Sin(y)	0.23	20.0
Gentec #16	Sin(x)Sin(y)	0.26	30.0
Gentec #17	Sin(x)Sin(y)	0.23	60.0
NPL01	Sin(x)	0.94	30.8

We have also made patterned substrates of gold, copper, silver or aluminum blanks using Schafer's precision micromachining capability. Unfortunately, it is difficult if not impossible to remove PS from machined metallic molds after casting. We are hopeful, however, that ethylene-chlorotrifluoroethylene (E-CTFE) can be molded using machined substrates giving us greater flexibility in providing patterned targets.

4.1.3. NIKE Low-Density Foam Targets

The primary NRL target design includes low-density foam. In the past, and to some extent now, we provided polyimide-covered CTMs to NRL and they would make RF foam to complete the target. During FY00, we developed the capability to make RF foam targets at Schafer so NRL resources could be freed for other tasks. Because our foam lab is in a clean room environment, the foams and foam targets we make at Schafer are generally cleaner and of better quality than those made in a chemistry lab at NRL. The

techniques we use are those that were developed at NRL and some of the equipment we use was supplied by NRL.

We have also begun production of foams with rippled surfaces. We form these foams against a mold of rippled polyimide or a patterned quartz substrate. The foam pattern matches the pattern on the mold fairly well; wavelengths match exactly and amplitudes are about two-thirds the mold amplitude (Fig. 4.1–5). We are starting work on making patterned foams directly on patterned polyimide that has been stretched onto a CTM. Thus we will have provided targets with flat polyimide and patterned foam, patterned polyimide and flat foam, and finally patterned polyimide with patterned foam.

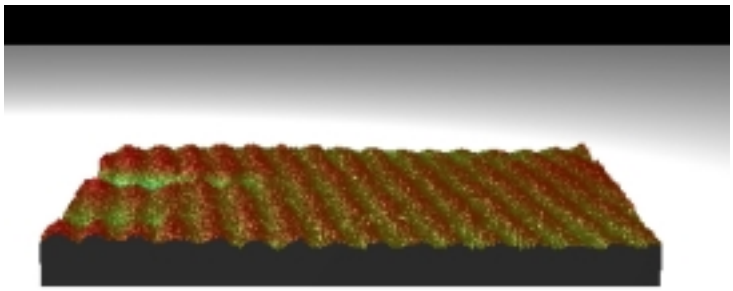

Fig. 4.1–5. Rippled surface on RF foam.

We are developing other kinds of foam to use for NRL NIKE targets. Much of the development is being done in conjunction with foam development for Sandia Albuquerque. NRL has primarily been interested in development of PS foams, TPX foams, and di-vinyl benzene foams. These efforts are mainly being done by Schafer at Sandia Albuquerque and are reported on in another section.

4.2. OMEGA LASER TARGETS

OMEGA laser targets are similar in nature and specifications to some NIKE laser targets. However, a large fraction of the OMEGA laser targets are multilayer films of at least two different polymers: PS and silicon doped polystyrene (Si-PS). The films are subsequently cut into much smaller discs and mounted for use as OMEGA laser targets.

We have found that the two polymers behave quite differently when they are processed to provide target films. One problem is that the two materials are soluble in the same solvents and there can be mixing at the layer boundary. Additionally, the silicon-doped PS material has a much lower molecular weight than the regular PS resulting in films which are very fragile and tend to crumble. Furthermore, the stresses associated with two layers of dissimilar polymer tend to cause fractures in the PS. Sometimes we

have trouble getting one polymer-solvent material to wet the underlying substrate. During the past year, we have tried several approaches to improving the quality of films we send to UR/LLE.

We have addressed the problem of interfacial mixing due to solvent solubility in several ways. First, we were successful in creating a well-defined boundary between layers by airbrushing the second layer onto the first. The solvent in the airbrushed layer dried before any of material in the underlying layer was dissolved. The resulting surface, however, was not smooth. The particles resulting from airbrushing left an orange peel texture to the surface with features larger than UR/LLE's specifications allowed. The orange peel effect may be mitigated by controlling the spray pressure, dilution, and droplet size, but increased smoothness seems to be accompanied by increased mixing at the layer boundary.

In order to ensure wetting, the surface energy of the casting surface must be greater than the surface tension of the polymer solution. Our normal solvent, toluene, has a surface tension of 27.9 mN/m and, when mixed with Si-PS, does not wet PS well. To facilitate wetting, we have used several techniques including heating the polymer solution, oxidizing the casting surface, and using a solvent with a lower surface tension. We have found that hexane, which has a surface tension of 17.9 mN/m, wets well, but causes microfractures to appear throughout the film. Decane with an intermediate surface tension has also been tried, but even with substrate heating, there are still microfractures and poor wetting. Our best results so far have been using di-isopropylether (IPE) as a solvent and applying the Si-PS/IPE solution under a pressure and temperature controlled environment where the temperature is elevated but the evaporation rate is slowed. There is still some swelling at the interface due to solvent mixing and subsequent off-gassing stresses the system.

Next year, we plan to try other CH polymers beside PS that can be kept more flexible than PS and, therefore, not be damaged by the stress of adding a second layer.

For further information, please contact T. Walsh (Schafer).

5. CRYOGENIC SCIENCE AND TECHNOLOGY DEVELOPMENT

The OMEGA laser at the University of Rochester/Laboratory for Laser Energetics (UR/LLE) and the National Ignition Facility (NIF) at Lawrence Livermore National Laboratory (LLNL) will need cryogenic targets. We devoted effort in support of the Inertial Confinement Fusion (ICF) laboratories to understand and control various solid fuel layer smoothing processes for both D_2 and deuterium-tritium (D-T) fuel. We designed equipment and test pieces for laboratory work in development of cryogenic targets for NIF, and we carried out design and planning activities for the NIF Cryogenic Target System (NCTS). This chapter reports some of the interesting technical results from these efforts in FY00.

5.1. ENHANCED CRYOGENIC LAYERING DEVELOPMENT

In natural beta-layering, the heat from tritium decay provides the energy to redistribute and smooth the D-T ice layer inside a cryogenic ICF capsule [5–1]. Deposition of energy in the D-T ice or D-T gas by infrared (IR) or microwave illumination offers the potential to accelerate the beta-layering process, to achieve smoother D-T ice surface finish, and to achieve layering in DD or hydrogen-deuterium (H-D) ice that does not have the tritium decay heat source of D-T.

5.1.1. IR-Enhanced Layering: Slow Cooldown Experiments

The most significant set of IR layering experiments conducted this fiscal year examined the effects of slow cooldown of H-D layers exposed to relatively high levels of IR illumination. The goal of these experiments was to determine a laser power and cooling rate that minimized layer degradation on cooling to 1.5 K below the triple point of H-D. In these experiments, IR radiation produced the volumetric heating instead of the tritium beta decay heating. By adjusting the laser power one can produce volumetric heating rates that are many multiples of the 50 mW/cc ($=Q_{D\text{-}T}$) beta decay generated heating rate. This set of experiments was made possible by the acquisition of a new IR laser. The output power of the new laser is approximately five times that available from the old F–center laser.

Figure 5.1–1 shows the layout for these experiments which have been described previously [5–2,5–3]. The first series of experiments was conducted at a fixed cooling rate of 20 mK every 3 minutes for laser powers (measured at the final coupling before the IR fiber enters the cryostat) ranging from 7 mW (1.4 $Q_{D\text{-}T}$) to 270 mW (54 $Q_{D\text{-}T}$). At this

cooling rate, the total cooldown time was 3–3/4 hours. Based on earlier surface roughness experiments, one would expect high laser power, or high volumetric heating rates, to help smooth the layer [5–4]. Indeed, at higher laser powers the layers were relatively smoother. However, the layers still degraded as the temperature was lowered. For the second set of experiments, the cooling rate was reduced by a factor of two to 10 mK every 3 minutes. Here the total cooling time is 7–1/2 hours. Figure 5.1–2 contains two images from one of these experiments. Figure 5.1–2(a) shows the layer shortly after it was formed near the triple point. Figure 5.1–2(b) shows the same layer after it had been cooled approximately 1.5 K below the triple point. The calculated rms surface roughness for both these images is 1.33 μm. The power spectra for these two images are plotted in Fig. 5.1–3. Similar results were achieved using a laser power of 150 mW (~30 $Q_{D\text{-}T}$). From these results, it appears promising that with a combination of slow cooling and IR heating, ice layers adequately smooth for NIF can be formed.

For further information, please contact Dr. D. Bittner (Schafer).

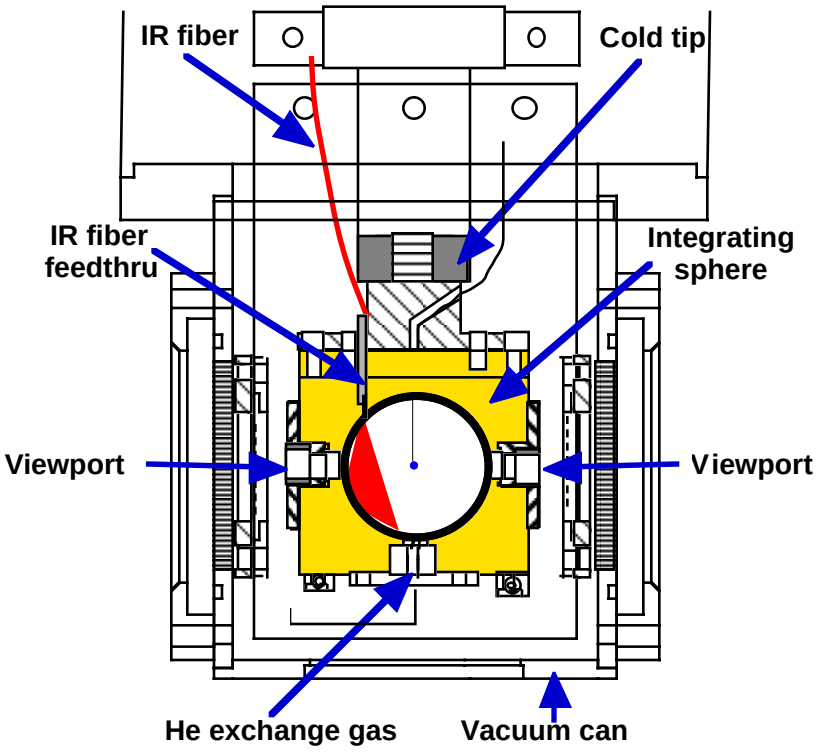

Fig. 5.1–1. Schematic diagram of IR optical fiber injection technique.

(a) T_{melt} – 0.1 K (b) T_{melt} – 1.5 K

Fig. 5.1–2. Images of a H-D layer after formation near the triple point (a) and at the end of a slow cooldown (b). The volumetric heating rate in the case was about 40 $Q_{D\text{-}T}$.

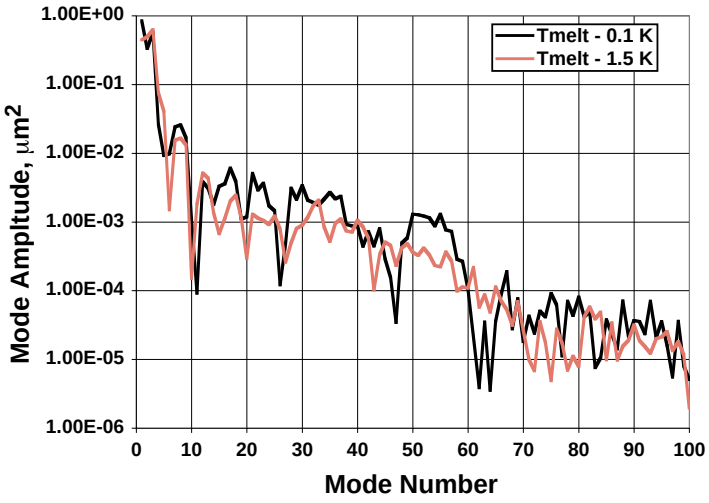

Fig. 5.1–3. Power spectra for the two images in Fig. 5.1–2. The rms roughness for both curves is 1.33 μm.

5.1.2. Beta Layering

It has long been clear that the final quality of layers formed by native β layering is sensitive to details of the initial layer growth. It has been reported previously [5–5] that cooling liquid D-T rapidly through the triple point usually results in a supercooled liquid. When the liquid freezes, it does so quickly and crystals nucleate from many points. Where the crystals meet, a grain boundary is formed. These boundaries affect the local surface roughness and severely degrade the layer quality. Native β layering does smooth

the layer somewhat after the initial freezing but is not able to completely overcome the grain boundary energy and remove all traces of the defect.

The technique used to mitigate the effects of supercooling is as follows. The D-T liquid is frozen and then slowly melted until only a small region of solid remains at the coldest point in the capsule. (For our experiments, this is near the fill tube.) Ideally, this solid region would be a single crystal of D-T, but we cannot directly determine or control the crystal nucleation with the current experiment. The suitability of the seed is determined empirically by the smoothness of the resulting layer. The temperature of the capsule is then lowered, allowing the growth/freezing front to propagate through the liquid in a controlled manner. We have determined that after the D-T has all solidified, it is best to wait for several hours at a constant temperature just below the triple point temperature of 19.73 K before cooling the layer to the final temperature. This allows for native β layering to remove low mode asymmetries.

Figures 5.1–4 and 5.1–5 are examples of two of the simpler types of layer growth observed. Shown are 125 μm layers in a 2-mm CD plastic capsule 40 μm thick. In Fig. 5.1–4 the solid first freezes in a narrow band like structure. As the temperature is lowered further the band widens until we finally end up with a moderately smooth layer.

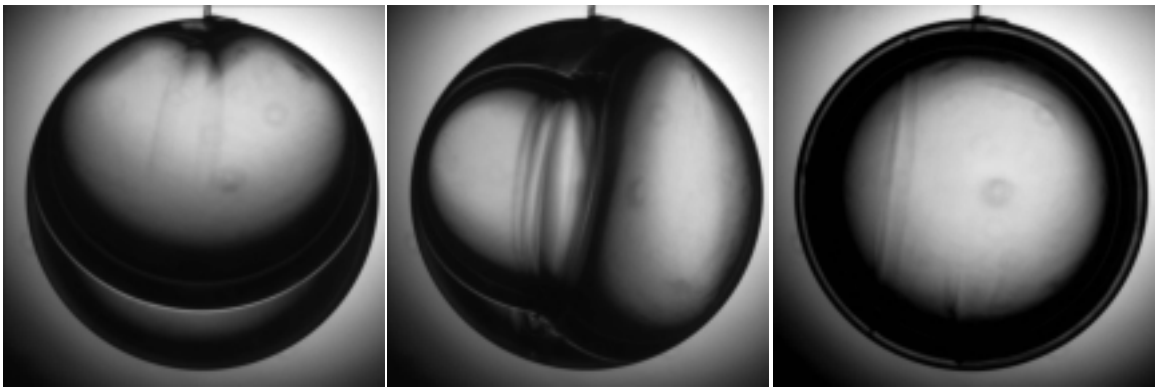

Fig. 5.1–4. Initial growth is in a longitudinal direction as seen in first figure on the left. Later in time, a band forms almost from pole to pole and begins to thicken. Finally, the layer is complete. (The bands are slightly out of focus. The left side of the band is on the farthest side of the shell, the right is on the near side.)

In Fig. 5.1–5 the growth habit is simpler. The solid advances from the fill tube in a symmetric fashion until it reaches the bottom of the shell. The defect observed at 5 o'clock in the last picture of Fig. 5.1–5 is a remnant of the boundary formed when the growth fronts meet.

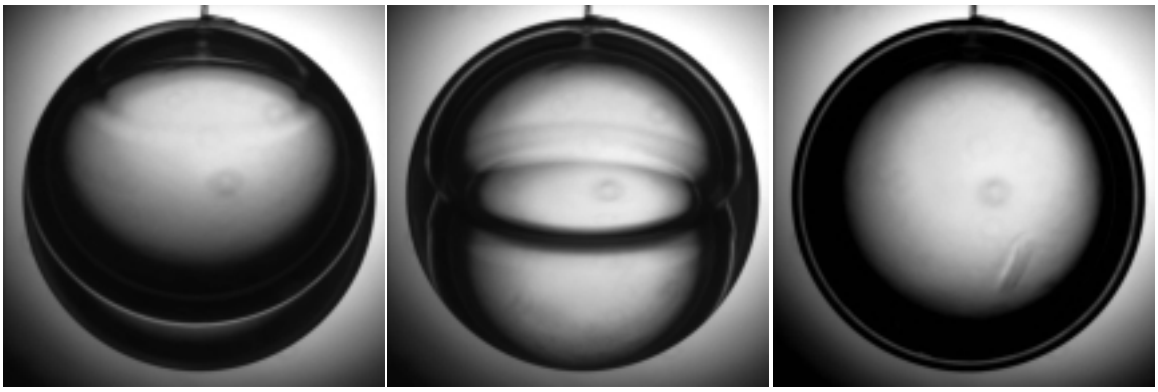

Fig. 5.1–5. Initial growth is almost axially symmetric. As the temperature continues to decrease the growth front moves down the shell. After completely solidifying this capsule forms a smooth layer.

This initial growth in Figs. 5.1–4 and 5.1–5 can be related to earlier work done with D_2 crystals on flat substrates [5–6,5–7]. Figures 5.1–6 and 5.1–7 are courtesy of Kozioziemski and Collins. Figure 5.1–6 is a crystal of D_2 between the roughening temperature of the (1100) facets and the triple point. The (0001) plane is not roughened. Crystals grow most rapidly along roughened facets, therefore this shape of crystal grows rapidly in a lateral direction and thickens slowly. This is the same behavior as exhibited in Fig. 5.1–5.

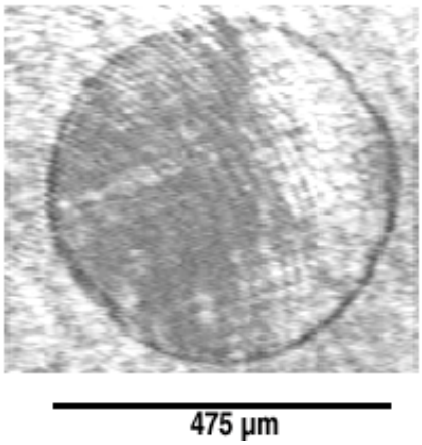

Fig. 5.1–6. A crystallite of D_2 with the c-axis perpendicular to the substrate. The crystallite is below the triple point temperature of D_2 but above the roughening temperature of the 1100 facets [5–6].

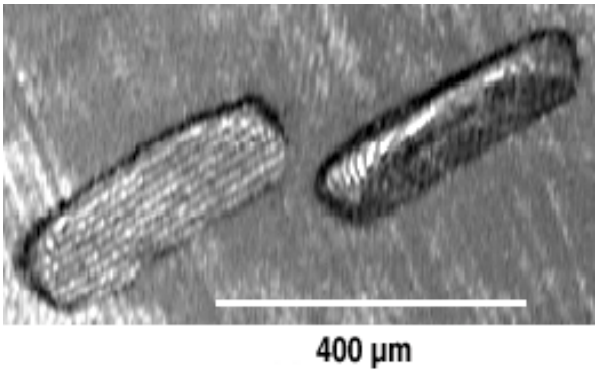

Fig. 5.1–7. A crystallite with the c-axis oriented at some unknown angle to the normal of the page. The short sides of the rectangular shape are (1100) facets [5–7].

Figure 5.1–7 is a D_2 crystal with its c-axis not perpendicular to the substrate. The long axis of the rectangle is the $\langle 1100 \rangle$ direction, the c-axis is some undetermined angle to the normal of the substrate and perpendicular to the $\langle 1100 \rangle$ direction. This form of crystal grows most rapidly along the $\langle 1100 \rangle$ direction and at an intermediate velocity in the perpendicular direction. This is the same type of growth observed in the series of

pictures in Fig. 5.1–4. A long narrow structure grows in a somewhat vertical fashion in the first picture of Fig. 5.1–4. In the second picture, we can see that the ends of the structure meet and that it has begun widening.

Figure 5.1–8 plots the minimum power spectral density observed for the series of layers formed during the runs of Figs. 5.1–4 and 5.1–5. There are large differences in the two sets of data, especially at the mid to high modes. This difference is largely due to the grain boundaries formed by the extra growth fronts of Fig. 5.1–4. The minimum rms surface roughness of the layer in Fig. 5.1–4 is 2.2 μm. The minimum rms of Fig. 5.1–5 is 1.1 μm. The growth habit of the layer in Fig. 5.1–5 is clearly preferable. Unfortunately, in our capsule, layers like Fig. 5.1–4 tend to be much more common. The process is stoichastic. It appears, however, that with care acceptably smooth D-T ice layers can be formed.

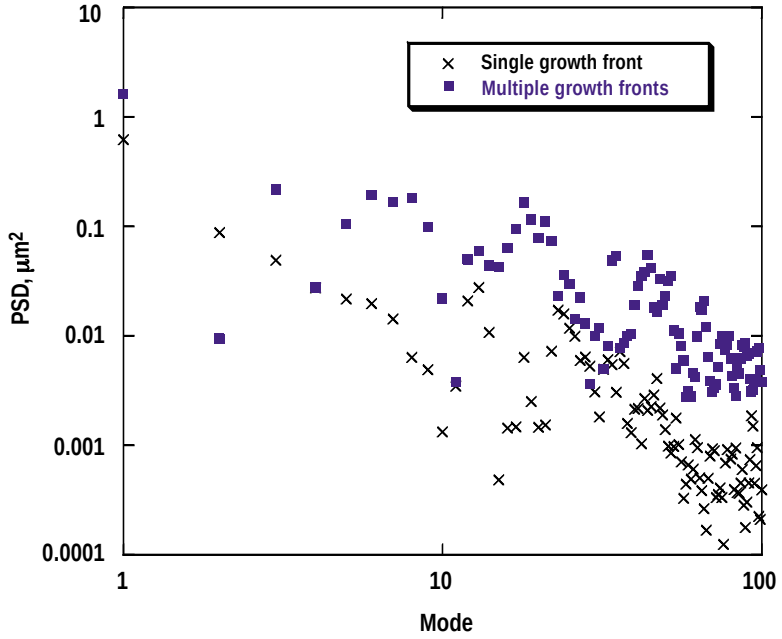

Fig. 5.1–8. The power spectra of the finished layers from Figs. 5.1–4 and 5.1–5 is very different. The power in some modes differ by an order of magnitude. The boxes are from the last image in Fig. 5.1–4, the Xs are from the last image in Fig. 5.1–5.

For further information, please contact Dr. J. Sater (Schafer).

5.2. BETA LAYERING SUPPORT AT LANL

Work by John Sheliak at Los Alamos National Laboratory (LANL) during FY00 included the completion of several tasks concerning the design, installation, and testing of

various elements of the cryogenic pressure loader (CPL) system. The assembly of all elements of the CPL has been completed and the system is currently in various stages of acceptance testing. Work also included the setup and startup of a new series of solid layering experiments that will be performed in order to examine the effects of D-T aging in a beryllium torus with a spherical surface/volume ratio. FY00 work also included comparison measurements of the surface roughness of a D-T solid layer inside a 2-mm sphere for images produced during experiments done at LLNL.

5.2.1. Completion of CPL Design, Installation, and Setup Tasks

The CPL system is a target filling and β-layering apparatus designed to test permeation fill operations with D-T, as well as measure tritium migration from the permeation cell apparatus to other regions within the cryostat and associated plumbing. The CPL will also permit the study of native β-layering in a permeation-filled ICF target under actual field conditions. The local control system (LCS) for the CPL apparatus was designed to provide automated control of the target insertion and layering sphere subsystems, automated control of pumps and valves used to perform D_2 and D-T fill operations, automated control of the optical apparatus used to position image acquisition optics, and automated computer acquisition of temperature and target image data. In addition to the CPL hardware and computerized instrumentation, an interface between the CPL LCS and the tritium facility instrumentation and control system (ICS) has been designed to allow tritium facility operators (FOs) to lock-out D-T and D_2 gas handling operations in the CPL glove box.

5.2.1.1. Accelerometer Motion Sync System. The motion synchronization electronics have been upgraded with the addition of filter and phase lock loop (PLL) circuitry, and several circuit adjustments that allow the system to operate at the 1.2 Hz CPL cryostat motion frequency. This upgrade extracts a “simple harmonic motion” signal from a very noisy and vibration-dominated accelerometer signal from the CPL cryostat. The accelerometer is mounted on the cryostat to monitor motion and vibration. Cryostat motion causes the image centroid and focus to shift from frame to frame, which can degrade the accuracy of the solid layer roughness measurement. When the accelerometer signal is processed, a simple harmonic motion signal is extracted, which is then used to produce a trigger signal synchronized to the zero crossing of the sinusoidal cryostat motion cycle. This signal then triggers the image acquisition system so that variations in frame-to-frame image position and focus are greatly reduced or eliminated. This is called PLL sychronization.

Figure 5.2–1 is a graph that compares the focal shift per image (motion along optical axis), for images acquired without synchronization and images acquired with motion synchronization. Fifty images were acquired for each sync state (non-sync and

PLL-sync), and the average focal shift was computed based on the amount of edge spreading in the images produced by motion induced defocusing. Normalization, in this case, is the average focal shift per image minus the average focal shift due to background vibration or noise. Background focal shift per image is measured with the cryostat off at room temperature for 50 acquired images. This graph shows that image-to-image focal variations due to cryostat motion can be reduced by 84% using this motion sync technique. The <0.1 μm focal variation obtained, when used with the f/3 lens, should give more than adequate resolution.

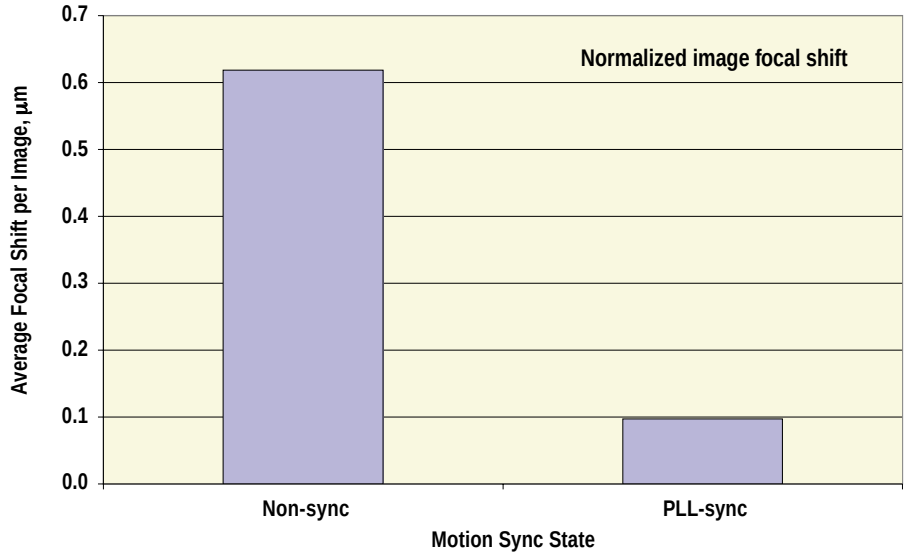

Fig. 5.2–1. Comparison of image focal shifts (motion along optical axis) for images acquired without motion synchronization (non-sync) and those acquired with motion sync (PLL-sync). Focal shift per image is computed by averaging the focal shift of 50 images, and normalization is performed by removing the focal shift due to background noise or vibration (cryostat off).

5.2.1.2. CPL Systems Integration and Testing. The hardware assembly and setup phases of systems integration of the CPL project have been completed; and systems integration is now in a phase of testing that will be followed by software development, facility interconnection, and finally D_2 and D-T filling. The process control/monitoring system computer was upgraded and reconfigured so that it can adequately perform valve control and system pressure and temperature monitoring. The data acquisition/control system computers have been brought on-line at the WETF facility where the CPL system has been installed. Preliminary testing of the field point (FP) module system that is used for controlling valve operation was completed, and the computer communication link established between the control computer and the FP modules located inside the CPL glove box. Additionally, network connections were established for both control system computers, allowing us to establish remote links with these systems for data downloading and software uploading.

An interlocking interface between the CPL control system and the WETF ICS was designed and installed to fulfill the tritium operations engineering requirements at the WETF. This system will allow the WETF FO to enable or disable certain D-T gas handling operations by the CPL control system as well as providing CPL status information to the FO. The interlocking includes ICS control of CPL access to the WETF gas handling system, as well as CPL access to tritium waste treatment system (TWTS). The CPL will also provide digital status bits to the ICS and FO, for "high pressure operations in progress" and "CPL run in progress" activities. The schematic of the overall system design of this system is shown in Fig. 5.2–2. The WETF facility ICS equipment is shown at the top of this schematic and interfaced to the CPL LCS by way of a VXI-based I/O subsystem or directly to the appropriate solenoid valve controls. The computer based VXI system was already in place for other types of interfacing done within the CPL system.

5.2.2. Image Analysis of D-T Solid Layer Inside a 2-mm Sphere

Detailed surface roughness comparison analyses were performed on an image of a D-T solid layer inside a 2-mm sphere, for an experiment done at LLNL. The layer was produced by a slow-freeze process and previously analyzed at LLNL using their new Gaussian Fit algorithm [5–8], which is suggested as a good measure of the D-T ice roughness. (Image and Gaussian data provided by J. Sater and LLNL.) Figure 5.2–3 shows the D-T solid layer inside a 2-mm plastic sphere. The image of the inside surface of the solid layer is shown as the thin white band inside the dark sphere. Figures 5.2–4(a) and 5.2–4(b) show the results of our analyses using the standard nonlinear (error function fit) edge trace algorithm. Figure 5.2–4(b) also includes the LLNL Gaussian fit data. Figure 5.2–4(a) shows graphs of the computed power spectra for the outside of the sphere, the outside edge of the white band, and the inside edge of the white band. Figure 5.2–4(b) shows the accumulative surface roughness determined with the nonlinear fit routine as well as the Gaussian fit routine. The accumulative roughness graph shows that the trace of the outer edge of the white band matches well the Gaussian fit trace. This is not inconsistent with LLNL's Gaussian analysis [5–8]. However, more work should be done to examine the relationship between the roughness calculated from the outer edge of the white band and the Gaussian roughness.

For more information, please contact J. Sheliak (GA at LANL).

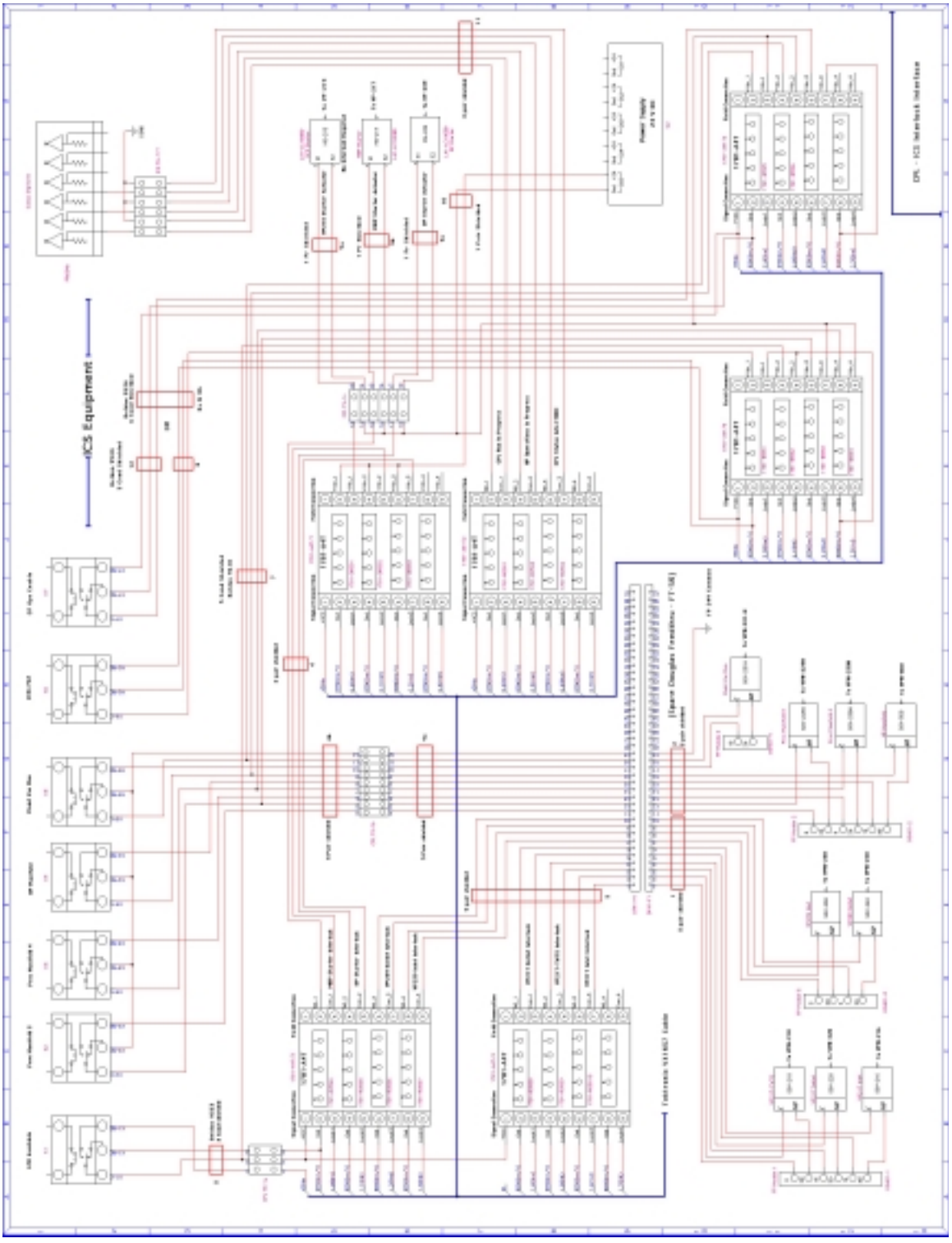

Fig. 5.2–2. Design schematic of the CPL-ICS interlocking interface with the ICS control relays and digital I/O channels shown at the top of the diagram. The diagram below the top row shows all the CPL side components.

Fig. 5.2–3. CCD image of a D-T solid layer inside a 2-mm plastic sphere. (Image and Gaussian data provided by J. Sater and LLNL.)

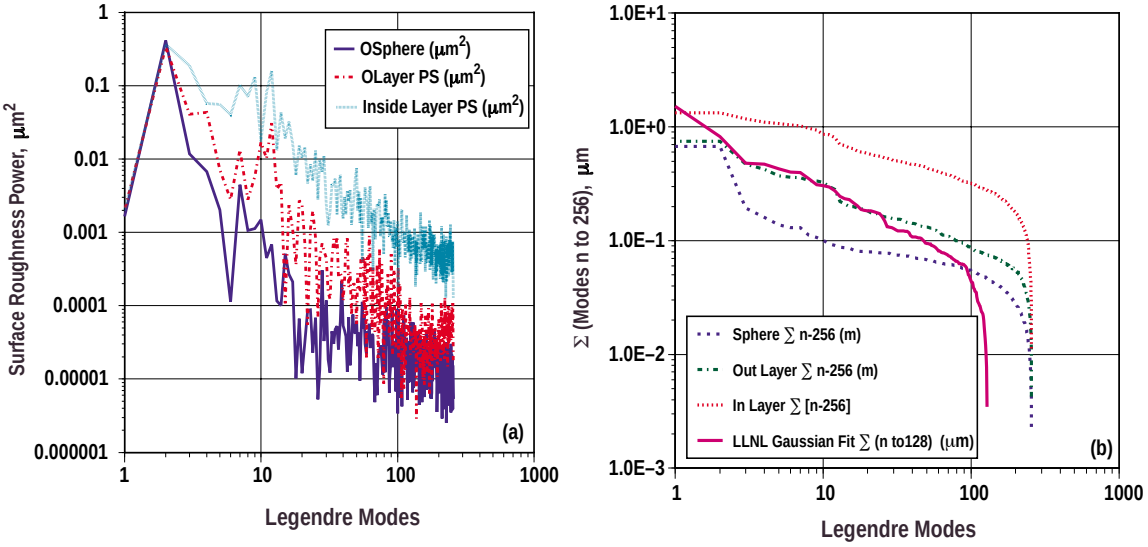

Fig. 5.2–4. Graphs showing the results of the nonlinear analysis (error function fit), and Gaussian analysis of the D-T solid layer and spherical target shown in Fig. 5.2–3. (a) shows the results of the Fourier Transform analyses of the inside and outside edges of the bright band shown in Fig. 5.2–3 edges, as well as the outside sphere edge, as determined by the error function fit. (b) is the sum of Legendre modes 1 to 256 for the traces in (a), in addition to the Gaussian fit data. The Gaussian data falls along the same curve as the error function data from the outside bright band edge.

5.3. REFERENCES FOR SECTION 5

[5–1] J.K. Hoffer and L.R. Foreman, Phys. Rev. Lett. **60**, 1310 (1988).

[5–2] Project Staff, "Inertial Confinement Fusion Target Component Fabrication and Technology Development Support, Annual Report to the U.S. Department of Energy, October 1, 1998 through September 30, 1999," J. Gibson, ed., General Atomics Report GA–A23240 (1999).

[5–3] D.N. Bittner, G.W. Collins, E. Monsler, and S. Letts, "Forming Uniform HD Layers in Shells Using Infrared Radiation," Fusion Technol. **35**, 244 (1999).

[5–4] Project Staff, "Inertial Confinement Fusion Target Component Fabrication and Technology Development Support, Annual Report to the U.S. Department of Energy, October 1, 1995 through September 30, 1996," M. Hoppe, ed., General Atomics Report GA–A22549 (1997).

[5–5] J. Sater et al., "Cryogenic D-T Fuel Layers Formed in 1 mm Spheres by Beta-Layering," Fusion Technol. **35**, 229 (1999).

[5–6] B.J. Kozioziemski, G.W. Collins, T.P. Bernat, "Crystal Growth and Roughening of Solid D_2," Fusion Technol. **31**, 482 (1997).

[5–7] B.J. Kozioziemski, unpublished data.

[5–8] J.A. Koch et al., Fusion Technology **38**, 123 (2000).

6. CRYOGENIC TARGET SYSTEM DEVELOPMENT FOR NIF

This year focussed on the design and procurement of a research cryostat for studying fuel layering in Inertial Confinement Fusion (ICF) targets filled to full density. This system is referred to as the deuterium test system (D_2TS). Work was also conducted on concepts to improve the commonality between the design concepts for the National Ignition Facility Cryogenic Target System (NCTS) and the Laser Megajoules Cryogenic Target System (LCTS). Additionally, design concepts for the NCTS were developed for operation with direct drive targets.

6.1. DEUTERIUM TEST SYSTEM

The D_2TS is a cryogenic system that allows full-sized National Ignition Facility (NIF) target assemblies to be filled to high density with D_2 or hydrogen-deuterium (H-D) fuel and allows fuel layering studies to be conducted. The target's capsule is filled via permeation in a high-pressure cell, not by a fill tube. This eliminates a major source of thermal asymmetry in the capsule's environment, so layering studies will be enhanced. Layering will be enabled by having optical access available to the target for infrared (IR) layering techniques and by electrical leads connected to the target to allow temperature shimming of the hohlraum. The high-density fill capability will produce thick fuel layers. These layers are more accessible for characterization in the spherical geometry of the capsule. The system can also prototype some items for the NCTS. Some of the key concepts of the NCTS that can be tested include: permeation filling of capsules inside of hohlraums with sealed laser entrance hole (LEH) windows, investigation of the effects of the cryostat cooling scheme on the vibration of the target, target transfer from the filling system to the insertion system, and cold transport of targets for extended distances.

The D_2TS operates on target assemblies, one at a time. These will typically consist of a target attached to a robust cylindrical base by a small number of sapphire or aluminum rods. A fine capillary will run from the target's hohlraum to the base. If desired, a thermal shroud can be slipped over the target and attached to the assembly. The D_2TS consists of eight main sub-systems, see Fig. 6.1–1: the main cryostat, the cryogenic target gripper, the permeation cell, the permeation cell housing and motion system (PCHMS), the permeation cell support and cooling system (PCSCS), the permeation cell plug remover (PCPR), the cryostat sliding mount, and the gate valves. Last year's report [6–1] described the overall concept for the D_2TS and the operations to be performed to permeation fill a target in the permeation cell and retrieve the target with the main cryostat.

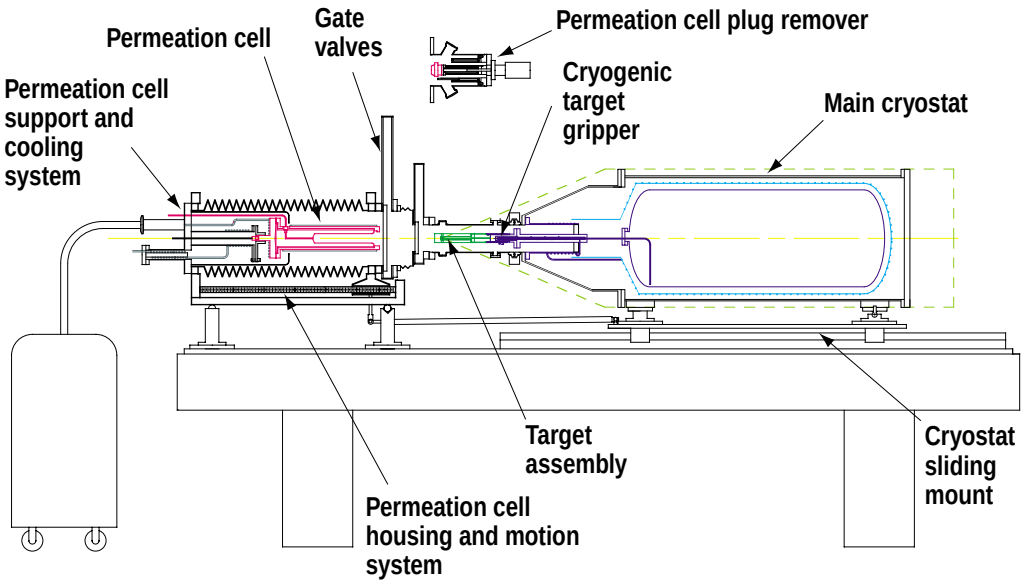

Fig. 6.1–1. The main cryostat of the D_2TS retrieves a target assembly from the permeation cell once the target has been filled and cooled.

This year, the D_2TS design underwent a number of design improvements before committing to fabrication with the overall concept remaining the same. The design was improved for better operability, better integration into the laboratory location (which was decided this year), and for ease of safety approval at Lawrence Livermore National Laboratory (LLNL). An example of an improvement for operability was to enlarge the inside diameter of the vacuum shroud of the main cryostat and the gatevalve on the vacuum shroud from 6 to 8 inches. This allowed the permeation cell to fit further into the vacuum shroud while being made shorter. The shorter permeation cell lowered the predicted cooldown time of the cell from 7.2 to 3.8 h. This will allow the time to fill and cool a target to be closer to a standard working shift. One example of better integration into the laboratory room was LLNL finding a larger room and optical table to locate the D_2TS. This allowed the cryostat sliding mount rails to be lengthened. This provides more room to install the PCPR onto the PCHMS. An example of design changes to ease safety approval was to modify the permeation cell dimensions and design pressure for a safety factor of four and to use an existing LLNL stock of certified high pressure fittings. The fabrication and procurement were started for all of the major subsystems except for the PCSCS. The PCSCS design drawings were nearly completed.

One of the key components of the D_2TS is the cryogenic target gripper. The design concept for the gripper and a photograph of it are contained in last year's report [6–1]. The gripper must make sound mechanical, electrical, and thermal connection to the target assembly base. The gripper also has to seal a gas line to the hohlraum's capillary that runs to the base of the target assembly. This line allows tamping gas and thermal exchange gas to be added to the hohlraum. This year, the gripper was tested for thermal,

electrical, and gas sealing performance. The gripper is shown installed in its test fixture in Fig. 6.1–2. The test fixture is placed into a vacuum chamber with cryogenic walls made from the interior space of a liquid nitrogen shielded, liquid helium dewar. The test fixture allows a surrogate target assembly and the gripper to be cooled to cryogenic temperature before the gripper grabs firmly onto the target assembly. The electrical connectors of the gripper support heaters and temperature sensors in the target assembly. These were used along with the gripper's own temperature sensor to measure the thermal performance of the gripper. The data reported on the gripper's performance is for cases where the cryogenic target gripper engaged the surrogate target assembly when both were cooled to cryogenic temperatures (~20 K) before the gripper fully engaged the target assembly.

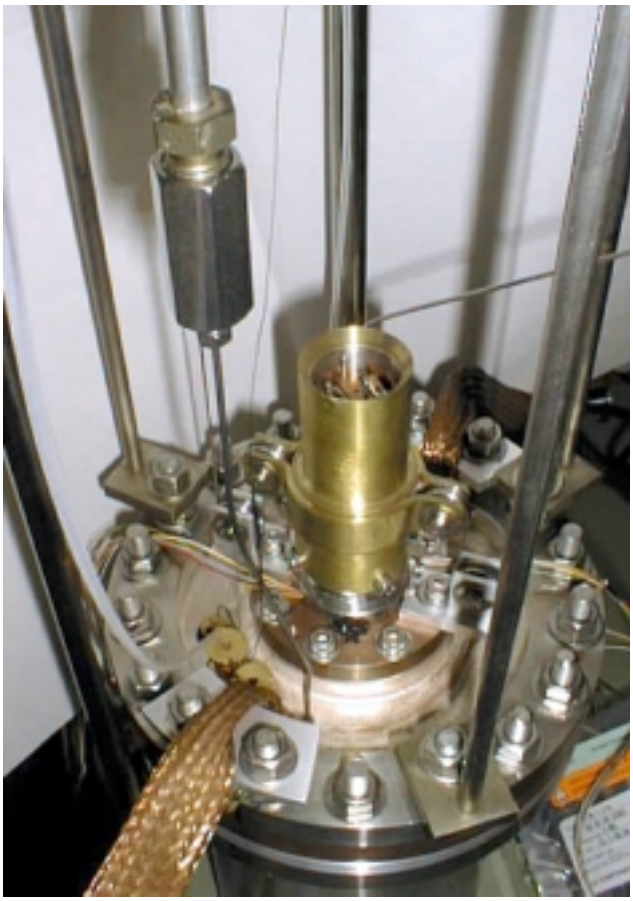

Fig. 6.1–2. The cryogenic target gripper is shown attached to the test fixture prior to the fixture being placed into a cryogenic walled vacuum space.

The thermal performance of the interface formed between the gripper and the target assembly base is shown in Fig. 6.1–3. This figure indicates that the temperature difference between the gripper and the base is only 4 K when the heat flowing through the interface is 1000 mW and the gripper temperature is 8 K. In this plot, the force used

by the gripper to hold the target base was 900 N. This allows for a 6.2 K temperature gradient between the target capsule and the target assembly base when the capsule is at the NIF point design target temperature of 18.2 K. The resistance of the electrical contact made between the gripper and base electrical connectors was measured to be ≤0.1 ohm. Through a series of three tests, the gas seal made by the gripper to the target base was measured to have a leak rate for helium of the less than 1×10^{-8} STD mbar l/s. The measured performance met the performance goals set out for the cryogenic target gripper.

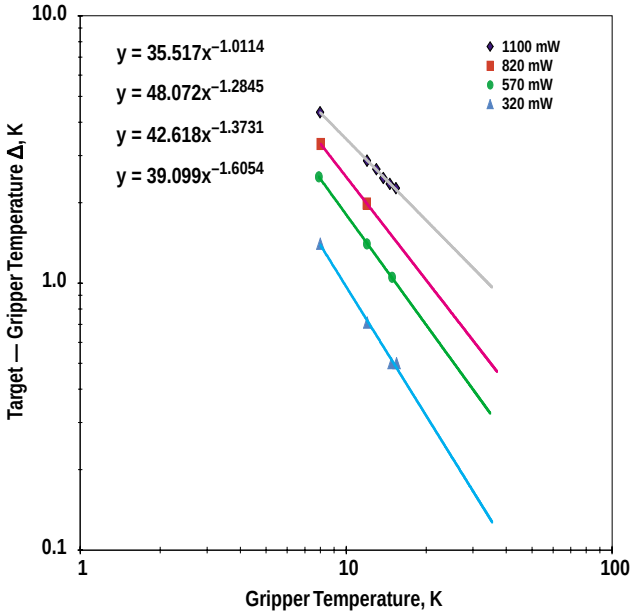

Fig. 6.1–3. The temperature dependence of the thermal performance of the cryogenic target gripper was measured. The curves correspond to different heat loads passing through the interface between the gripper and the target base. The force used to hold the target base was 900 N.

6.2. NIF AND LMJ CRYOGENIC TARGET SYSTEM COMMONALITY

The strengths and weaknesses of the "1A" type concept for the NCTS and the French concept for the LCTS were investigated. A table of strengths and weakness of the concepts was prepared. A primary strength of the "1A" is the ability to layer multiple targets at once, which allows the concept to meet the required shot rate, given the current understanding of the required layering time. A primary weakness of the "1A" is the large amount of contaminated and activated mass that is transported during normal operation. A primary strength of the LCTS concept is the small amount of contaminated and activated mass that is transported during normal operation. A primary weakness of the LCTS concept is that only one target can be layered at a time, which does not allow the

concept to meet the required shot rate, given the current understanding of the required layering time.

More than 20 hybrid concepts between the "1A" concept for the NCTS and LCTS concept were developed. The goal was to look for concepts that could be used at both NIF and Laser Megajoules (LMJ) with the system at each site being the same or only slightly modified. An example of one of the hybrids is shown in Fig. 6.2–1. In this example, the targets are filled and individually loaded onto target insertion cryostats (TIC) for transport to the laser facility and for layering of the target fuel as is the case for the NCTS concept. The targets on TICs are installed onto the target positioner of the target chamber, remotely and using vacuum vessels, as is the case for the LCTS concept. The target positioner would use the LCTS concept. The TIC size would be reduced to help implement this hybrid.

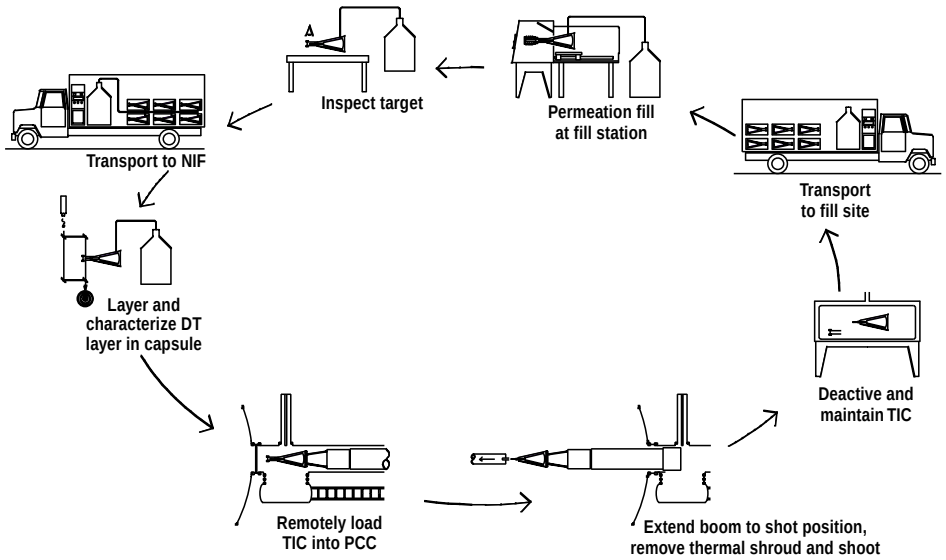

Fig. 6.2–1. One of the more than 20 concepts that were developed for a cryogenic target system (CTS) that is a hybrid between the French concept for the LCTS and the "1A" concept for NIF. The PCC is the LCTS target positioner.

6.3. DIRECT DRIVE CONCEPTS FOR THE NIF CRYOGENIC TARGET SYSTEM

The original "1A" concept for the NCTS was not suited for fielding direct drive targets. This was due to the fill station using a vacuum chamber with a room temperature wall to contain the permeation cell. The direct drive target is deliberately mounted on a support with low thermal conductivity so that the beta-layering process will produce a sufficiently spherical fuel layer. Heat from the beta-decay of the D-T fuel is removed from the target capsule by conduction through a low pressure of helium gas surrounding

the target and linking it to a cold source. For the original "1A" concept, this gives two unacceptable pathways for moving a direct drive target from the permeation cell to the TIC. One is to do the transfer in vacuum. This removes the cooling source for the target, which will rapidly heat up and burst from the pressure generated by the heated fuel in the target. The other is to put gas in the vacuum chamber of the permeation cell. Unfortunately, this thermally links the target to the room temperature walls of the vacuum chamber much more strongly than to the cold source provided by the cold head of the TIC or the cell. Thus, the direct drive target again heats and burst due to internal pressure generated by the fuel in the capsule. The indirect drive target can utilize the vacuum chamber design since the filled capsule is contained within a gas filled hohlraum. This provides for removal of the beta-decay heat.

The "1A" concept can be modified to handle direct drive targets. The fill station must use a cryostat instead of a vacuum chamber to house the permeation cell. Additionally, the TIC is placed in a vacuum tight chamber to allow it to couple to the fill station without letting the exterior atmosphere into the fill station cryostat. The fill station cryostat can be filled with low pressure helium gas to maintain thermal contact with the target without thermally connecting the target to a high temperature surface. This allows the target to be transferred from the permeation cell to the TIC without damaging the target by heating it. This is the same concept that was successfully implemented in the OMEGA Cryogenic Target Handling System. The overall cycle for fielding a cryogenic target is shown in Fig. 6.3–1 and an enlargement of the fill station with the TIC retrieving a target is shown in Fig. 6.3–2.

For further information, please contact Dr. N. Alexander (GA).

6.4. REFERENCE FOR SECTION 6

[6–1] Project Staff, "Inertial Confinement Fusion Target Component Fabrication and Technology Development Support, Annual Report to the U.S. Department of Energy, October 1, 1998 through September 30, 1999," J. Gibson, ed., General Atomics Report GA–A23240 (1999).

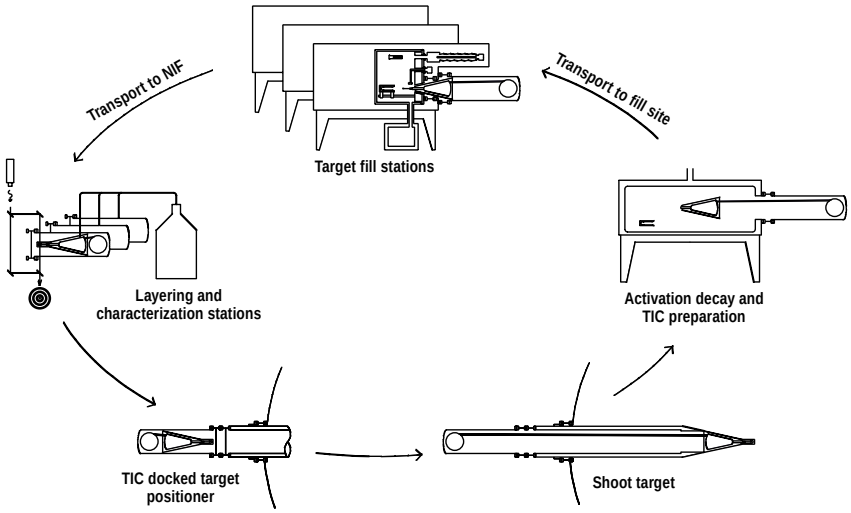

Fig. 6.3–1. To allow fielding of direct drive targets, the "1A" concept for the NIF CTS can be modified so that the permeation cell used to fill the target is housed in a cryostat and the TIC is housed in a vacuum chamber.

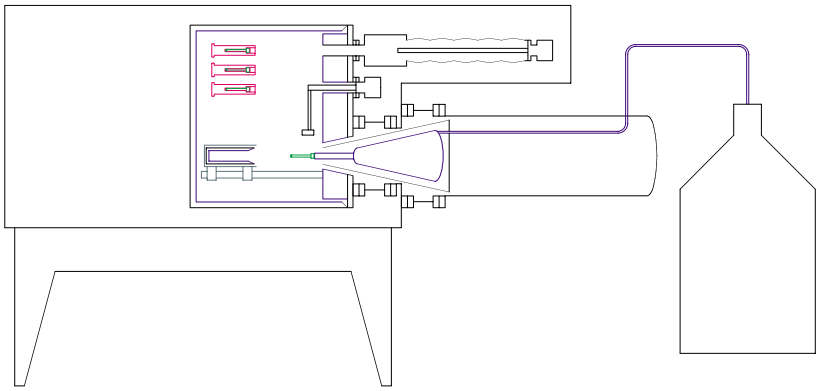

Fig. 6.3–2. This figure shows the use of a cryostat for the fill station so that direct drive targets may be transferred onto the TIC.

7. FY00 PUBLICATIONS

Besenbruch, G.E., Alexander, N.B., Baugh, W.A., Bernat, T.P., Collins, R.P., Boline, K.K., Brown, L.C., Gibson, C.R., Goodin, D.T., Harding, D.R., Lund, L., Nobile, A., Schultz, K.R., and Stemke, R.W., "Design and Testing of Cryogenic Target Systems," Proc. Int. Conf. on Inertial Fusion Science and Applications '99, edited by C. Labaune, W.J. Hagan, K.A. Tanaka (Elsevier, Paris, 2000) p. 921; General Atomics Report GA–A23299 (1999).

Gibson, C.R., Alexander, N.B., Del Bene, J.V., Goodin, D.T., and Besenbruch, G.E., "Cryogenic Target System for Z-Pinch Machines," presented at Cryogenic Engineering Conf. and Int. Cryogenic Materials Conf., Montreal, 1999, Advances in Cryogenic Engineering **45**, 1127 (2000); General Atomics Report GA–A23188 (1999).

Hoppe, M.L., "Large Glass Shells from GDP Shells," presented at 13th Target Fabrication Meeting, Catalina Island, 1999, Fusion Technology **38**, 42 (2000); General Atomics Report GA–A23356 (2000).

McQuillan, B.W., Paguio, S., "Living Radical Polymerization of Trimethylsilylstyrene," presented at 13th Target Fabrication Meeting, Catalina Island, 1999, Fusion Technology **38**, 108 (2000); General Atomics Report GA–A23352 (2000).

Nikroo, A., Elsner, F.H., Czechowicz, D.G., Gibson, J.B., Grant, S.E., Greenwood, A.L., Hoppe, M.L., Husband, D.O., McQuillan, B.W., Miller, W.J., Pontelandolfo, J.M., Steinman, D.A., Stephens, R.B., Schultz, K.R., Takagi, M., "Capsule Production and Development for ICF Experiments," Proc. Int. Conf. on Inertial Fusion Science and Applications '99, edited by C. Labaune, W.J. Hagan, K.A. Tanaka (Elsevier, Paris, 2000) p. 917; General Atomics Report GA–A23228 (1999).

Nikroo, A., Pontelandolfo, J.M., "Fabrication of Thin Walled Glow Discharge Polymer Shells," presented at 13th Target Fabrication Meeting, Catalina Island, 1999, Fusion Technology **38**, 58 (2000); General Atomics Report GA–A23339 (2000).

Project Staff, "ICF Target Support Highlights," a monthly report General Atomics Report GA–A22688 (2000).

Project Staff, "Inertial Confinement Fusion Target Component Fabrication and Technology Development Support, Annual Report to the U.S. Department of Energy, October 1, 1998 through September 30, 1999," J.B. Gibson, ed., General Atomics Report GA–A23240 (1999).

Silke, G.W., Gibson, C.R., "Remote Handling of Cryogenic Targets for the OMEGA Laser System," in electronic Proc. 8th Int. Top. Mtg. on Robots and Remote Systems, Pittsburgh, 1999, Session 11 (ANS, Carnegi Mellon, 1999); General Atomics Report GA–A23039 (1999).

Stephens, R.B., Mroczkowski, T., Gibson, J.B., "Seeing Shell Wall Fluctuations," presented at 13th Target Fabrication Meeting, Catalina Island, 1999, Fusion Technology **38**, 132 (2000); General Atomics Report GA–A23348 (2000).

8. ACKNOWLEDGMENT

This report of work was prepared for the U.S. Department of Energy under Contract No. DE-AC03-95SF20732.